

Three-dimensional separation induced by a convected disturbance

By H. ATIK, C. Y. KIM AND J. D. A. WALKER

Department of Mechanical Engineering and Mechanics, Lehigh University,
19 Memorial Drive West, Bethlehem, PA 18015, USA

(Received 13 August 2002 and in revised form 9 April 2003)

A three-dimensional inviscid velocity distribution is selected to mimic the flow produced at the wall by a three-dimensional vortex convected above an infinite wall. The main interest is in determining the viscous response of the boundary layer on the wall to the imposed pressure distribution. It is demonstrated that complex effects occur in the boundary layer (including the formation of zones of apparent recirculation) that eventually lead to separation. Solutions are obtained in both a conventional Eulerian frame of reference and with a three-dimensional Lagrangian method. The separation takes the form of a sharply focused eruptive tongue of fluid in a manner consistent with modern asymptotic theories of three-dimensional separation, which indicate the boundary-layer solution will develop a singularity in the absence of interaction with the external flow. The unsteady separation structure is similar to that in two dimensions when viewed in the appropriate direction. The possible relevance of the results to the dynamics of turbulent boundary layers is described.

1. Introduction

Unsteady separation processes at high Reynolds number have been of interest for decades. The pioneering work of Van Dommelen & Shen (1980, 1982) revealed how boundary-layer separation initiates in two-dimensional flows for motion past an impulsively started circular cylinder. When the external pressure field is prescribed, the separation process is usually heralded by the appearance of recirculating eddies and shortly thereafter the boundary layer erupts at a streamwise location near the eddy in a narrow plume. As anticipated by Van Dommelen & Shen (1982) and Elliott, Cowley & Smith (1983), the phenomenon is generic for two-dimensional flows, as evidenced by much subsequent work (see, for example, Cowley, Van Dommelen & Lam 1990; Degani, Walker & Smith 1998). A detailed and clear description of the separation process has been given by Van Dommelen (1991); in this process, a fluid particle on the zero vorticity line within the boundary layer eventually becomes squashed in the streamwise direction to zero thickness thereby provoking an eruption, which in two dimensions appears as a knife-edge. Thus, in the absence of a formulation which permits an interaction with the external flow, the boundary-layer solution develops a singularity at separation. Because of the abrupt nature of the process and the sharp focusing in the streamwise direction that occurs, it proves very difficult to structure a calculation procedure using a conventional Eulerian formulation that can accurately describe the details of the phenomenon. For this reason, separation events are now usually computed using a Lagrangian formulation, as originally described by Van Dommelen & Shen (1982) (see, for example, Degani *et al.* 1998).

The situation in unsteady three-dimensional flows at high Reynolds numbers is rather more complicated and relatively few reliable numerical solutions exist. A theoretical description of unsteady separation in three-dimensional flows has been given by Van Dommelen & Cowley (1990). The theory predicts that separation will occur along a U-shaped ridge in the form of a narrow eruptive tongue, which extends to an infinite distance from the wall (on the boundary-layer scale) as a fluid particle is compressed to zero thickness at separation. In a plane normal to both the wall and the erupting ridge, the separation process was shown to be similar to that in two-dimensional flows (Van Dommelen & Cowley 1990). The practical problem of calculating a three-dimensional flow is considerably more complex than in two dimensions and, in view of the theoretical description of unsteady separation, it was anticipated that such a calculation would be very difficult using a conventional Eulerian formulation with a fixed spatial mesh. It may be noted that for two-dimensional flows, Adams, Conlisk & Smith (1995) and Xiao, Burggraf & Conlisk (1997), for example, have considered methods which use a time-dependent adaptive grid that refines the mesh in a region where separation is developing. A key issue here concerns what feature of the developing Eulerian field should be used to guide a dynamic mesh refinement. Adams *et al.* (1995) considered several criteria, such as the streamwise gradient of the displacement thickness and the blowing velocity at the boundary-layer edge, and were able to obtain good comparisons with previous results obtained by Peridier, Smith & Walker (1991), who used a Lagrangian method. However, at present, the Lagrangian approach appears to be the optimal adaptive scheme for two-dimensional flows. In three-dimensional separating flows, the issues of how to structure an adaptive grid in the Eulerian description and what features of the solution should be used to guide refinement are at least an order of magnitude more complex. It seems unlikely that an Eulerian method which accurately resolves the structure of the unsteady three-dimensional separation process will be feasible in the near future. In this study, the Lagrangian equations are solved numerically for a number of cases where the boundary-layer solution develops a separation singularity. A method of determining when the singularity occurs is described and it is demonstrated that the calculated results are in general agreement with the theory of Van Dommelen & Cowley (1990).

The particular problems addressed here were motivated by a proposed model of the events that lead to production of new turbulence near a surface (Smith *et al.* 1991). It is commonly accepted (Head & Bandyopadhyay 1981; Robinson 1991; Smith *et al.* 1991; Smith & Walker 1997) that the hairpin vortex is an important structure in the turbulent boundary layer. A critical issue in turbulent wall-bounded flows is the determination of the physical process whereby new hairpin vortices are created near the surface; this process is often referred to as regeneration. Such events have been observed in a variety of experimental studies (see, for example Smith & Walker 1997), as well as in detailed examinations of the results of direct numerical simulations of turbulence at low Reynolds numbers (Robinson 1991). On the basis of various experimental studies, computational simulations in two-dimensional flows and an existing theory of three-dimensional separation (Van Dommelen & Cowley 1990), Smith *et al.* (1991) described a hypothetical process in which a moving hairpin vortex could provoke a local three-dimensional separation of the turbulent wall layer. It was argued that this phenomenon would take the form of a thin tongue of fluid, containing elevated levels of vorticity, that would erupt from the wall layer. In a subsequent interaction, the erupting tongue would be expected to roll over into a new hairpin vortex. It may be noted that the theoretical study of Smith & Burggraf

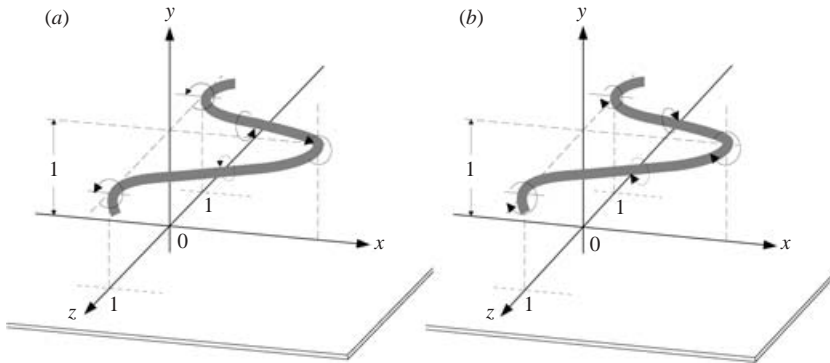


FIGURE 1. Schematics of a three-dimensional vortex convecting above an infinite plane wall for (a) positive circulation $+\kappa$, (b) negative circulation $-\kappa$.

(1985) had also anticipated that similar events would occur in deep transition and approaching turbulence in laminar boundary layers.

A goal of this study is to develop a computational means to calculate the onset of such an eruption and to verify some conjectural aspects of the process described by Smith *et al.* (1991). Because the main objective here is to determine the viscous response of the boundary layer to a moving three-dimensional disturbance, the external inviscid flow was selected in an *ad hoc* manner in order to mimic certain features of the flow near the wall due to a moving hairpin vortex.

2. The inviscid flow

The rectilinear vortex is a limiting case of vortex motion in two dimensions where the vorticity is tightly concentrated in a small core region. If such a vortex of positive circulation κ is located at a distance a from an infinite plane wall in an otherwise stagnant fluid, inviscid theory predicts that the vortex will convect to the right with constant speed $\kappa/2a$ at constant height a above the wall, driven by the image vortex below the wall. Let all lengths and velocities be made dimensionless with respect to a and $\kappa/2a$, respectively. In a frame of reference convecting with the vortex, the wall appears to move with constant speed -1 to the left. The boundary layer associated with this two-dimensional problem has previously been considered by Walker (1978) and Peridier *et al.* (1991), who showed that the adverse pressure gradient due to the vortex rapidly induces boundary-layer separation in the form of an abrupt sharply focused eruption.

Consider now the more complex configuration shown in figure 1(a) where a three-dimensional vortex of positive circulation is above the wall in an otherwise stagnant fluid; the instantaneous shape shown is taken to be periodic in the spanwise direction with symmetry planes at $z=0$ and ± 1 , etc. In general, a vortex with this initial configuration will start to convect and deform immediately owing to self-induced motion and the action of the image vortex below the plate. During this evolution, portions of the vortex may either recede or approach the plate and, once a vortex exhibits three-dimensional distortions, it is generally not possible to find solutions which describe a convecting invariant form. The evolution and trajectory of such a vortex can be calculated through a numerical integration of the Biot-Savart law, provided certain assumptions are made concerning the nature of the flow in the vortex core. Many examples of such calculations exist in the literature (see, for example, Moore

1972; Leonard 1980; Dhanak & DeBernardinis 1981; Ersoy & Walker 1987; Hon & Walker 1991). The integrations can be very time-consuming as the vortex develops into complex shapes (Smith *et al.* 1991) and, in addition, can involve significant levels of numerical error. It was, therefore, convenient to select an analytical external inviscid velocity which mimics the distribution that would be expected to be produced instantaneously by the vortex configuration shown in figure 1(a). In this way, it was possible to concentrate on the viscous flow development using a well-defined analytic external velocity field without the additional complications associated with a Biot-Savart integration.

The velocity field is selected as a generalization of the problem considered by Walker (1978) and is representative of the velocity field produced by the vortex depicted in figure 1(a) near the wall and in a frame of reference convecting with the vortex. Let (x, y, z) denote Cartesian coordinates measuring dimensionless distances (referred to a) in the streamwise, normal and spanwise directions, respectively, with corresponding velocity components (u, v, w) . The external dimensionless (referred to $\kappa/2a$) velocity field is taken to be

$$U_\infty(x, z) = -1 + U_e(x, z), \quad W_\infty(x, z) = W_e(x, z), \quad (2.1)$$

for $-\infty < x < \infty$ and $0 \leq z \leq 1$, where

$$U_e(x, z) = \frac{4}{\{x - f(z)\}^2 + 1}, \quad W_e(x, z) = -\frac{4f'(z)}{\{x - f(z)\}^2 + 1}, \quad (2.2a, b)$$

and

$$f(z) = \frac{1}{2}(1 + \cos(\pi z))c. \quad (2.3)$$

The inviscid flow is assumed to convect without change of shape and, in a frame of reference moving with the disturbance, the wall is taken to move uniformly to the left with speed -1 . Note that the velocity field described by equation (2.1) is irrotational.

In the model flow, the function $f(z)$ is the projection of the vortex in figure 1 in the (x, z) -plane, while the parameter c is a measure of the level of three-dimensional distortion in the vortex, with $c = 0$ being the two-dimensional case; the physical streamwise length of the distortion is then ca . At the base of each of the vortex legs

$$U_\infty = -1 + \frac{4}{x^2 + 1} \quad \text{at } z = \pm 1, \quad (2.4)$$

while in the symmetry plane through the vortex head

$$U_\infty = -1 + \frac{4}{(x - c)^2 + 1} \quad \text{at } z = 0. \quad (2.5)$$

Thus on $z = 0$ and $z = \pm 1$, the streamwise velocity is the same as for the rectilinear vortex (Peridier *et al.* 1991), but note that the vortex centre on $z = 0$ is displaced downstream to $x = c$. The spanwise velocity in equation (2.2) has flow away from the plane $z = 0$ and toward a maximum at $z = \pm 0.5$ and then decreases toward $z = 1$; the strength of the spanwise flow is modelled by the positive parameter c . For increasing c , the external velocity distribution becomes more three-dimensional and the adverse spanwise pressure gradient more severe.

If the sense of circulation in figure 1(a) is reversed, the resulting vortex has negative rotation and, in general, will propagate in the negative x -direction. This case for a rectilinear vortex has previously been considered by Doligalski & Walker (1984) and Degani *et al.* (1998). For a rectilinear vortex of strength $-\kappa$ at a distance a from the

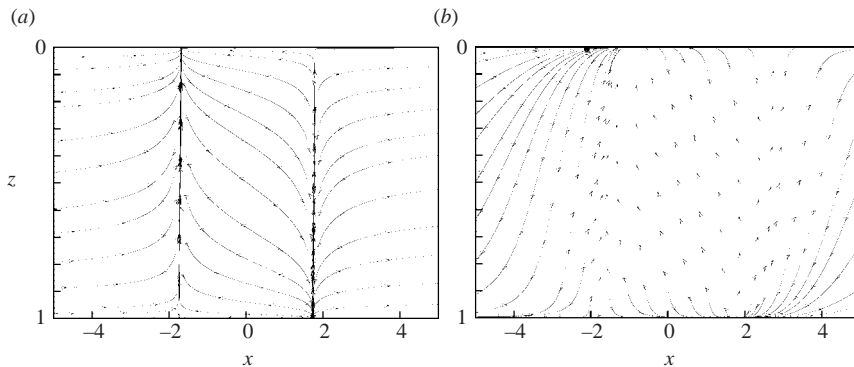


FIGURE 2. Inviscid streamlines near the wall in a frame of reference moving with the vortex. (a) $\kappa < 0$, $c = 0.05$, (b) $\kappa < 0$, $c = 1.0$.

wall, the vortex will propagate in the negative x -direction with velocity $-\kappa/2a$. If a uniform flow of speed U_0 is superimposed to the right, the vortex is then convected to the right with velocity $V_c = \alpha U_0$, where α is the fractional convection rate defined as $\alpha = 1 - \kappa/(2aU_0)$. In a frame of reference convecting with the vortex, the flow speed at infinity is $(1 - \alpha)U_0$, and if this is used as a characteristic speed to define dimensionless variables, the external velocity induced by the moving two-dimensional vortex near the wall is given by equation (2.4) multiplied on the right-hand side by -1 , for all z (Doligalski & Walker 1984). In the convected frame, the wall appears to move progressively to the left with speed $\beta = \alpha/(1 - \alpha)$. As shown by Degani *et al.* (1998), the boundary layer under the moving vortex separates from the surface for α less than a critical value of $\alpha_c \approx 0.58$ ($\beta \approx 1.38$), with the separation event becoming stronger and occurring sooner for decreasing α . On the other hand, for a relatively weak vortex ($\alpha > 0.58$), the influence of the moving wall dominates the viscous flow near the wall and separation does not occur.

Here, the case where the three-dimensional vortex is of the type illustrated in figure 1(b) with the rotation reversed (from figure 1a) is now embedded in a uniform flow to the right. The model inviscid flow is similar to that described by equation (2.1), but now the signs are reversed. The general form of the external dimensionless velocity field given by (2.1) can be written

$$U_\infty(x, z) = \text{sgn}(\kappa)\{-1 + U_e(x, z)\}, \quad W_\infty(x, z) = \text{sgn}(\kappa)W_e(x, z), \quad (2.6)$$

for either case. The inviscid flow for $\kappa < 0$ is believed to be similar to the motion produced near the wall by a convected hairpin vortex (Smith *et al.* 1991). The limiting inviscid streamlines on the surface for $\kappa < 0$ are shown in figure 2 for two cases corresponding to $c = 1$ and $c = 0.05$ (an almost two-dimensional case) in a frame of reference moving with the vortex. Note that stagnation points occur in both symmetry planes. The additional variable that occurs for $\kappa < 0$ is the wall speed β , and results for $\beta = 0.25$ and $\beta = 0.50$ will be considered here; the former case models a slow-moving vortex close to the wall, while the latter case represents a faster-moving vortex. The streamwise external velocity for $\kappa < 0$ on the symmetry planes is given by equations (2.4) and (2.5), with each term on the right-hand side multiplied by -1 .

The pressure gradients imposed on the boundary layer may be evaluated from

$$-\frac{\partial p_\infty}{\partial x} = U_\infty \frac{\partial U_\infty}{\partial x} + W_\infty \frac{\partial U_\infty}{\partial z}, \quad -\frac{\partial p_\infty}{\partial z} = U_\infty \frac{\partial W_\infty}{\partial x} + W_\infty \frac{\partial W_\infty}{\partial z}, \quad (2.7)$$

and it is easily confirmed that both gradients are independent of $\text{sgn}(\kappa)$. It can be shown that $\partial p_\infty/\partial x = 0$ on the projection of the vortex core $x = f(z)$, where a local minimum in p_∞ occurs for fixed z . Whether the streamwise pressure gradient is regarded as adverse depends on the local flow direction. For $\kappa > 0$, the pressure increases in the flow direction for all $x > f(z)$ which is thus a region of adverse streamwise pressure gradient. On the other hand, for $\kappa < 0$, the external velocity field reverses direction and the zone of adverse streamwise pressure gradient occurs behind the vortex $x < f(z)$. For all cases considered here, a separation event occurred in a region where both the streamwise and spanwise pressure gradients are adverse. It can be shown that $\partial p_\infty/\partial z$ vanishes along one or more curves in the (x, z) -plane depending on the magnitude of c ; one of these curves intersects $x = f(z)$ at a location denoted by (x_{min}, z_{min}) where a pressure minimum occurs. For the cases with $\kappa > 0$, the external flow moves toward $z = 1$ and an adverse spanwise pressure gradient occurs for $z > z_{min}$. Conversely for $\kappa < 0$, the external flow is toward $z = 0$ and an adverse spanwise pressure gradient occurs for $z < z_{min}$. Thus, although the pressure distribution is the same for both situations, separation is expected on either side of (x_{min}, z_{min}) depending on $\text{sgn}(\kappa)$ in a region where both pressure gradients are adverse (see, also Walker 2003). The speed of the moving wall also has an important influence on the location of separation, and on whether it occurs at all.

3. The boundary layer

In order to determine the viscous response to the inviscid motions described in §2, the viscosity was taken to be switched on suddenly at $t = 0$. Define a Reynolds number by $Re = |\kappa|/\nu$, where ν is the kinematic viscosity; for large Re and time $t > 0$, a thin unsteady boundary layer develops on the wall. The three-dimensional boundary-layer equations in dimensionless variables are

$$\frac{\partial u}{\partial t} + u \frac{\partial u}{\partial x} + v \frac{\partial u}{\partial y} + w \frac{\partial u}{\partial z} = U_\infty \frac{\partial U_\infty}{\partial x} + W_\infty \frac{\partial U_\infty}{\partial z} + \frac{\partial^2 u}{\partial y^2}, \quad (3.1a)$$

$$\frac{\partial w}{\partial t} + u \frac{\partial w}{\partial x} + v \frac{\partial w}{\partial y} + w \frac{\partial w}{\partial z} = U_\infty \frac{\partial W_\infty}{\partial x} + W_\infty \frac{\partial W_\infty}{\partial z} + \frac{\partial^2 w}{\partial y^2}, \quad (3.1b)$$

$$\frac{\partial u}{\partial x} + \frac{\partial v}{\partial y} + \frac{\partial w}{\partial z} = 0, \quad (3.1c)$$

where y and v are scaled in the usual way with respect to $Re^{-1/2}$. The boundary conditions are

$$u = -1 \quad \text{for } \kappa > 0, \quad u = -\beta \quad \text{for } \kappa < 0, \quad v = w = 0 \quad \text{at } y = 0, \quad (3.2)$$

where κ refers to the sense of circulation shown in figure 1; in addition,

$$u \rightarrow U_\infty(x, z), \quad w \rightarrow W_\infty(x, z) \quad \text{as } y \rightarrow \infty, \quad (3.3)$$

to match the external flow and

$$u \rightarrow U_R, \quad (v, w) \rightarrow 0 \quad \text{as } x \rightarrow \pm\infty. \quad (3.4)$$

Here, U_R denotes the two-dimensional boundary-layer solution at upstream and downstream infinity in a frame of reference moving with the vortex; this is given by

$$U_R = -1 \quad \text{for } \kappa > 0; \quad U_R(\rho) = -\beta + (1 + \beta)\text{erf}(\rho) \quad \text{for } \kappa < 0, \quad (3.5)$$

where ρ is the Rayleigh variable defined by $\rho = y/(2\sqrt{t})$ (Doligalski & Walker 1984).

In the Eulerian formulation of the problem, it is convenient to define normalized velocities $U(x, y, z, t)$ and $W(x, y, z, t)$ according to

$$u(x, y, z, t) = U_R(\rho) + \text{sgn}(\kappa)U_e U, \quad w(x, y, z, t) = \text{sgn}(\kappa)W_e W, \quad (3.6)$$

where U_e and W_e are defined in (2.2). The boundary conditions for U and W are

$$(U, v, W) = 0 \quad \text{at } y = 0; \quad (U, W) \rightarrow 1 \quad \text{as } y \rightarrow \infty, \quad (3.7)$$

for all z .

Conditions are also required in the spanwise direction and near the symmetry planes (i.e. as $z \rightarrow 0, 1$); the velocity components may be written in the form (Ersoy & Walker 1987; Puhak, Degani & Walker 1995)

$$u = u(x, y, t) + O(\tilde{z}^2), \quad v = v(x, y, t) + O(\tilde{z}^2), \quad w = \tilde{z}\theta(x, y, t) + O(\tilde{z}^3), \quad (3.8)$$

where \tilde{z} denotes z and $z-1$ near the planes $z=0$ and $z=1$, respectively. Equations (3.1) take the following form on the symmetry planes

$$\frac{\partial u}{\partial t} + u \frac{\partial u}{\partial x} + v \frac{\partial u}{\partial y} = U_\infty \frac{dU_\infty}{dx} + \frac{\partial^2 u}{\partial y^2}, \quad (3.9a)$$

$$\frac{\partial \theta}{\partial t} + u \frac{\partial \theta}{\partial x} + v \frac{\partial \theta}{\partial y} + \theta^2 = U_\infty \frac{d\Theta_\infty}{dx} + \Theta_\infty^2 + \frac{\partial^2 \theta}{\partial y^2}, \quad (3.9b)$$

$$\frac{\partial u}{\partial x} + \frac{\partial v}{\partial y} + \theta = 0, \quad (3.9c)$$

where u and v satisfy the same conditions as in equation (3.2) at the wall and, in addition, $\theta = 0$ at $y = 0$. Also

$$u \rightarrow U_\infty(x), \quad \theta \rightarrow \Theta_\infty(x) \quad \text{as } y \rightarrow \infty, \quad (3.10)$$

where $U_\infty(x)$ and $\Theta_\infty(x)$ in equations (3.9) and (3.10) are given by

$$U_\infty(x) = \text{sgn}(\kappa) \{-1 + U_e(x)\}, \quad \Theta_\infty(x) = \text{sgn}(\kappa)\Theta_e(x), \quad (3.11)$$

which represent equations (2.6) in the limit $z \rightarrow 0$ or $z \rightarrow 1$; here, $\Theta_e(x)$ can be evaluated analytically in (2.2b) by taking the limit of $W_e(x, z)/z$ as $z \rightarrow 0$ or $z \rightarrow 1$.

The boundary-layer flow develops for all $t > 0$ once the no-slip condition is suddenly applied at $t = 0$. The initial flow is conveniently described in terms of the following Rayleigh variables

$$\rho = \frac{y}{2\sqrt{t}}, \quad V = \frac{v}{2\sqrt{t}}, \quad (3.12)$$

which were introduced into the equations on the symmetry planes and in the interior. The equations in terms of the variables (U, V, W) and (x, ρ, z, t) are easily obtained (Atik 2002).

4. Lagrangian formulation

The boundary-layer solution for a given external flow was integrated forward in time, and complicated flow topologies were soon found to develop. Eventually, all solutions considered evolved toward separation with strong updrafts occurring in a very localized zone. In the Lagrangian description, the independent spatial variables (ξ, η, ζ) denote the positions of fluid particles at some initial instant at $t = t_0$ (i.e. $(x, y, z) = (\xi, \eta, \zeta)$ at $t = t_0$). Each fluid particle is then identified for $t > t_0$ by its current position (x, y, z) and its velocity components (u, v, w) , which are all functions

of (ξ, η, ζ, t) . In the present study, calculations were initially started in Eulerian coordinates at $t=0$, then switched over at a time $t=t_0$ to the Lagrangian formulation and subsequently continued to separation at $t=t_s$. The Lagrangian calculations are computationally intensive, and it is more efficient to calculate the initial stages of the motion using the conventional Eulerian formulation when the solution is still well behaved. As strong local outflows develop and the solution begins to evolve toward a singularity, the Lagrangian formulation is needed. The switchover time t_0 is arbitrary to some extent; it should be selected well enough in advance of t_s so that the Eulerian field is still smooth, but not so far in advance of t_s that remeshing of the Lagrangian scheme is required (Degani *et al.* 1998).

The Lagrangian equations for a three-dimensional boundary layer with a steady mainstream flow are of the form (Van Dommelen & Cowley 1990)

$$\frac{\partial \phi}{\partial t} = U_\infty \frac{\partial \Phi_\infty}{\partial x} + W_\infty \frac{\partial \Phi_\infty}{\partial z} + \frac{\partial^2 \phi}{\partial y^2}, \quad (4.1)$$

where $\phi = u$ or w and $\Phi_\infty = U_\infty$ or W_∞ , respectively; U_∞ and W_∞ are given by equations (2.6). In Lagrangian coordinates, the normal gradient in equation (4.1) is defined by (Van Dommelen & Cowley 1990)

$$\frac{\partial}{\partial y} = (x_\zeta z_\eta - x_\eta z_\zeta) \frac{\partial}{\partial \xi} + (x_\xi z_\zeta - x_\zeta z_\xi) \frac{\partial}{\partial \eta} + (x_\eta z_\xi - x_\xi z_\eta) \frac{\partial}{\partial \zeta}, \quad (4.2)$$

and the Jacobian of the transformation J is constant, namely

$$J(x, y, z; \xi, \eta, \zeta) = \frac{\partial(x, y, z)}{\partial(\xi, \eta, \zeta)} = \begin{vmatrix} x_\xi & x_\eta & x_\zeta \\ y_\xi & y_\eta & y_\zeta \\ z_\xi & z_\eta & z_\zeta \end{vmatrix} = 1, \quad (4.3)$$

where the subscripts denote partial derivatives; this is the continuity equation in Lagrangian coordinates. The set of equations (4.1) is completed with

$$\frac{\partial x}{\partial t} = u, \quad \frac{\partial z}{\partial t} = w. \quad (4.4)$$

To obtain the boundary conditions, note that the motion at upstream and downstream infinity (i.e. for $x = \xi = \pm\infty$) is a two-dimensional plane parallel flow and here $y = \eta$ for all t in Lagrangian coordinates. Consequently, the conditions are

$$u = U_R, \quad w = 0 \quad \text{as } \xi \rightarrow \pm\infty, \quad (4.5)$$

where U_R is given by (3.5) with ρ replaced by $\eta/(2\sqrt{t})$. As $\eta \rightarrow \infty$, the external conditions for u and w are defined by (2.6). At the wall ($y = \eta = 0$), u and w must satisfy conditions (3.2). Finally, fluid particles on the wall initially remain there, but their streamwise positions will change with time, i.e.

$$x(\xi, \eta, \zeta, t) = \xi - \beta(t - t_0), \quad z(\xi, \eta, \zeta, t) = \zeta \quad \text{at } \eta = 0, \quad (4.6)$$

where $\beta = 1$ for $\kappa > 0$ and is a specified value for $\kappa < 0$.

The solution was advanced in time by solving (4.1) and (4.4) for u , w , x and z subject to the above boundary conditions. At any instant, the normal distance $y(\xi, \eta, \zeta, t)$ of fluid particles from the surface can be evaluated from the continuity equation (4.3), which is a first-order equation for y . The characteristics are curves of constant x and z and are defined by the subsidiary equations for (4.3), i.e.

$$\frac{d\xi}{x_\zeta z_\eta - x_\eta z_\zeta} = \frac{d\eta}{x_\xi z_\zeta - x_\zeta z_\xi} = \frac{d\zeta}{x_\eta z_\xi - x_\xi z_\eta} = \frac{dy}{1}. \quad (4.7)$$

The characteristic curves for a given time t denote the initial locations of a group of fluid particles which have all arrived at a specific value of x and z ; each characteristic is therefore a space curve which originates at the wall and traces outward toward the boundary-layer edge. The solution of (4.7) may be written

$$y(\xi, \eta, \zeta, t) = \int_{\text{wall}}^{(\xi, \eta, \zeta)} \frac{ds}{\sqrt{(x_\xi z_\eta - x_\eta z_\xi)^2 + (x_\xi z_\zeta - x_\zeta z_\xi)^2 + (x_\eta z_\xi - x_\xi z_\eta)^2}}, \quad (4.8)$$

where s denotes a variable measured along a characteristic curve $x(\xi, \eta, \zeta, t) = \text{constant}$ and $z(\xi, \eta, \zeta, t) = \text{constant}$, starting from the wall ($\eta = y = 0$), and passing through the point (ξ, η, ζ) ; this expression gives the normal distance from the wall of a fluid particle which started at (ξ, η, ζ) at time t_0 . If a singularity develops at a later time (say, at $t = t_s$) at a location denoted $(\xi, \eta, \zeta, t) = (\xi_s, \eta_s, \zeta_s, t_s)$, then

$$x_\zeta z_\eta - x_\eta z_\zeta = x_\xi z_\zeta - x_\zeta z_\xi = x_\eta z_\xi - x_\xi z_\eta = 0. \quad (4.9)$$

As discussed by Van Dommelen & Cowley (1990), this condition occurs when the vectors ∇x and ∇z become parallel at a point, namely,

$$\nabla x = \lambda \nabla z, \quad (4.10)$$

for some constant λ (to be found) so that the Jacobian J in (4.3) vanishes. For oblique coordinates in the (x, z) -plane defined by $q = x - \lambda z$, it follows that $\nabla q = 0$. In this direction, a fluid particle is compressed to zero thickness (Van Dommelen & Cowley 1990; Van Dommelen 1991), and the separation process is similar to that in two dimensions. This direction in the (x, z) -plane will subsequently be referred to as the q -direction, while that normal to it is referred to as the q_n -direction. To compensate for this compression process, the fluid particle at separation must grow in the normal direction, by continuity. A particle is therefore eventually squeezed out of the boundary layer, being displaced an infinite distance from the wall (on the boundary-layer scale) toward the outer inviscid-flow region. In this process, a singularity evolves in the normal velocity v at that streamwise and spanwise location, indicating that the boundary layer starts to erupt over a region of zero thickness in the q -direction. The criterion (4.10) for evaluation of a singularity is not easily implemented in a computational scheme and an alternative method of detecting the singularity in the computations is described in the Appendix.

The Lagrangian formulation for the symmetry planes at $z = 0$ and 1 is defined similarly. Particles on a symmetry plane remain there for all time, except perhaps near isolated points. The spanwise particle position \check{z} (see (3.8)) is anticipated to be a regular function of time which can be written in the form

$$\check{z}(\xi, \eta, \zeta, t) = \check{\zeta} \check{z}(\xi, \eta, t) + \dots, \quad (4.11)$$

where $\check{\zeta}$ denotes ζ near $\zeta = 0$ and $\check{\zeta}$ denotes $\zeta - 1$ near $\zeta = 1$; evidently

$$\frac{\partial \check{z}}{\partial \xi} = \frac{\partial \check{z}}{\partial \eta} = 0 \quad \text{at} \quad \zeta = 0, 1, \quad (4.12)$$

and it follows from (4.3) that on the symmetry planes, the Jacobian is of the form

$$J = z_\zeta J_2 = \check{z}(\xi, \eta, t) J_2, \quad (4.13a)$$

where J_2 denotes the two-dimensional Jacobian on each of the symmetry planes, defined by

$$J_2 = x_\xi y_\eta - x_\eta y_\xi. \quad (4.13b)$$

It is easily shown that the boundary-layer equations on the symmetry planes in (3.9) are given in Lagrangian coordinates by

$$\frac{\partial \phi}{\partial t} = -\lambda_1 \phi + U_\infty \frac{d\Phi_\infty}{dx} + \lambda_2 + \frac{\partial^2 \phi}{\partial y^2}, \quad (4.14)$$

accompanied by

$$\frac{\partial x}{\partial t} = u, \quad \frac{\partial \tilde{z}}{\partial t} = \theta \tilde{z}, \quad (4.15a, b)$$

where $\phi = u$ or θ and $\Phi_\infty = U_\infty$ or Θ_∞ , respectively. U_∞ and Θ_∞ and their derivatives are known functions of x , defined by (3.11), and λ_1 and λ_2 are given by

$$\lambda_1 = \lambda_2 = 0 \quad \text{for } \phi = u; \quad \lambda_1 = \theta, \quad \lambda_2 = \Theta_\infty^2 = \Theta_e^2 \quad \text{for } \phi = \theta. \quad (4.16)$$

In addition, the normal gradient is given by

$$\frac{\partial}{\partial y} = \frac{1}{J_2} \left(x_\xi \frac{\partial}{\partial \eta} - x_\eta \frac{\partial}{\partial \xi} \right), \quad (4.17)$$

and the continuity equation (3.9c) for the symmetry planes is $J_2 \tilde{z} = 1$. Note that J_2 and \tilde{z} are initially unity at $t = t_0$ from the initial condition $(x, y)_{t=t_0} = (\xi, \eta)$, but J_2 changes with time as \tilde{z} changes according to (4.15). The boundary conditions for the equations on the symmetry planes are

$$u = -1 \quad \text{for } \kappa > 0, \quad u = -\beta \quad \text{for } \kappa < 0; \quad \theta = 0 \quad \text{at } \eta = 0, \quad (4.18a)$$

$$(u, \theta) \rightarrow (U_\infty, \Theta_\infty) \quad \text{as } \eta \rightarrow \infty; \quad (u, \theta) \rightarrow (U_R, 0) \quad \text{as } \xi \rightarrow \pm\infty, \quad (4.18b)$$

where U_R is given by equation (3.5) with ρ replaced by $\eta/(2\sqrt{t})$, and the streamwise positions on the wall of the fluid particles are

$$x = \xi - \beta(t - t_0) \quad \text{at } \eta = 0. \quad (4.19)$$

At any time step, the normal distance $y(\xi, \eta, t)$ can be calculated according to

$$y(\xi, \eta, t) = \int_{\text{wall}}^{(\xi, \eta)} \frac{J_2}{\sqrt{x_\xi^2 + x_\eta^2}} ds, \quad (4.20)$$

which is similar to (4.8), but the integral is now along a characteristic $x(\xi, \eta, t) = \text{constant}$ on either symmetry plane, starting from the wall ($\eta = y = 0$), and passing through the point (ξ, η) . For a singularity to develop in the x -field on either of the symmetry planes at a subsequent time $t = t_s$ at a location $(\xi, \eta) = (\xi_s, \eta_s)$, the condition $x_\xi = x_\eta = 0$ must occur (Puhak *et al.* 1995). In all of the present calculations, a singularity occurred, but always in the interior $0 < z < 1$ rather than on either symmetry plane.

It is convenient for computational purposes to work in domains of finite extent and, for the Eulerian problem, the streamwise and normal coordinates x and ρ defined in the ranges $(-\infty, \infty)$ and $(0, \infty)$ were transformed to the finite ranges $(-1, 1)$ and $(0, 1)$, respectively, by

$$x = c_x \tan(\pi \hat{x}/2), \quad \rho = c_y \tan(\pi \hat{\rho}/2). \quad (4.21)$$

The spanwise coordinate is defined in $0 \leq z \leq 1$ and a transformation is not necessary. Here, c_x and c_y are the streamwise and normal expansion factors, respectively, which control the physical grid spacings in each direction; smaller values of c_x and c_y

imply grids in the physical domains which are concentrated near $x=0$ (i.e below the vortex) and $y=0$ (i.e. at the wall). The two Lagrangian independent variables ξ and η (defined in the ranges $(-\infty, \infty)$ and $(0, \infty)$) and the dependent Lagrangian variables x and y (defined in the ranges $(-\infty, \infty)$ and $(0, \infty)$), respectively, were also transformed to the finite ranges in the computational domain according to

$$\xi = c_x \tan(\pi\hat{\xi}/2), \quad \eta = c_y \tan(\pi\hat{\eta}/2), \quad (4.22a)$$

$$x = c_x \tan(\pi\hat{x}/2), \quad y = c_y \tan(\pi\hat{y}/2). \quad (4.22b)$$

The other independent and dependent variables ζ and z for the spanwise coordinate range from 0 to 1. Here, c_x and c_y are the streamwise and normal expansion factors similar to those used in Eulerian coordinates; as a result, the computational coordinates have $-1 \leq (\hat{\xi}, \hat{x}) \leq 1$ and $0 \leq (\hat{\eta}, \zeta, z) \leq 1$.

5. Numerical methods

The boundary-layer equations in both Eulerian and Lagrangian coordinates were solved using a Crank–Nicolson method and a simple ADI (alternating–direction–implicit) method for sweeping the mesh at a given time with a second-order accurate upwind–downwind difference scheme for terms involving the first-order partial derivatives of x and z in (4.1). The method is similar to that described by Peridier *et al.* (1991) and Degani *et al.* (1998), but is second-order accurate in both time and space (Atik 2002).

The numerical calculations were started impulsively from rest ($t=0$) in computational Eulerian coordinates $(\hat{x}, \hat{\rho}, z)$, using the transformed forms of (3.1) for U, V, W , in addition to (3.9) for the symmetry planes, using the transformations (4.21). During the course of an iteration at each time step, the normal velocity V was computed by using a Simpson’s integration method. Later, at some time $t=t_0$, the calculations were switched to computational Lagrangian coordinates $(\hat{\xi}, \hat{\eta}, \zeta)$ and then continued until the evolution of a separation singularity at t_s ; the calculated Eulerian velocity field was used as the initial flow field at t_0 for the Lagrangian calculations. The equations used in the Lagrangian coordinates are the transformed forms of (4.1)–(4.4) for $\phi = u$ or w , in addition to (4.14)–(4.17) for the symmetry planes, with the computational coordinates given in (4.22).

Let t_f be the time at which a given Eulerian calculation fails; the switchover time t_0 in general was chosen as $t_0 > t_f/2$, but as close as possible to t_f provided that the Eulerian solution field was still sufficiently smooth. This is because calculations in the Lagrangian frame are very time-consuming, particularly in three dimensions. At the switchover time, the spatial meshes were matched as follows. Since $y = 2\sqrt{t_0}\rho = \eta$, then

$$2\sqrt{t_0}c_{y,E} \tan(\pi\hat{\rho}/2) = c_{y,L} \tan(\pi\hat{\eta}/2). \quad (5.1)$$

Thus, if $c_{y,L} = 2\sqrt{t_0}c_{y,E}$, the grids will match at the switchover time t_0 , where $c_{y,E}$ and $c_{y,L}$ are the normal expansion coefficients used in the Eulerian and Lagrangian coordinates, respectively. The values of c_x and c_y were selected pragmatically and typical values used in the calculations where $c_x = 1.0$ and $c_{y,E} = 1.0$.

Upon completion of the first sweep for $\phi_{i,j,k} = u_{i,j,k}$ and $w_{i,j,k}$ of the entire mesh by solution of a sequence of tridiagonal matrix problems along lines of constant $\hat{\xi}, \hat{\eta}$ and ζ , the streamwise and spanwise particle positions in the current time plane (t)

were calculated from the following finite-difference approximation to (4.4)

$$\hat{x} = \hat{x}^* + \Delta t \overline{\sigma u}, \quad z = z^* + \Delta t \overline{w}, \quad (5.2)$$

at a typical mesh point (i, j, k) , where

$$\sigma = \frac{2 \cos^2(\pi \hat{x}/2)}{\pi c_x}. \quad (5.3)$$

The overbar denotes a simple average value between the current and previous time planes; the asterisk represents the value at the previous time plane $(t - \Delta t)$. Similarly, on the symmetry planes, sweeps for $\phi_{i,j} = u_{i,j}$ and $\theta_{i,j}$ along lines of constant $\hat{\xi}$ and $\hat{\eta}$ were followed by advancing the solution of (4.15) for the new streamwise particle positions and the Jacobian J_2 , respectively; since $J_2 \hat{z} = 1$, (4.15b) can be written as

$$\frac{J_2 - J_2^*}{\Delta t} = -\overline{J_2 \theta}, \quad (5.4)$$

evaluated at a typical mesh point (i, j) . The iteration process was continued at a time step in order to achieve a specified minimum error in computing Φ or ϕ at each mesh point, i.e. $|1 - \phi^p/\phi| < \epsilon$, where ϕ^p is the previous iterate and ϵ is a specified relative error, taken here to be 10^{-6} . Note that this condition requires a tight level of convergence at each step. With successive iterates of $\phi_{i,j,k}$ converged at every mesh point, the numerical integration was then advanced to the next time plane $t + \Delta t$; typically, 4 to 6 iterations were required per time step.

During the course of a Lagrangian calculation, contours of \hat{x} , z , u , w and instantaneous streamlines were periodically plotted to see if any severe wiggles or distortions occurred. The purposes of these periodic examinations were: (i) to check out whether any unrealistic situations or numerical instabilities had developed in the calculation and (ii) to determine if a remeshing of the entire grid mesh was necessary in Lagrangian coordinates. One important feature of Lagrangian calculations for the developing boundary-layer flow is the behaviour of the contours of constant x (or constant \hat{x}) and z . When these fields develop a stationary point according to the criterion

$$\left(\frac{\partial \hat{x}}{\partial \zeta} \frac{\partial z}{\partial \hat{\eta}} - \frac{\partial \hat{x}}{\partial \hat{\eta}} \frac{\partial z}{\partial \zeta}, \quad \frac{\partial \hat{x}}{\partial \hat{\xi}} \frac{\partial z}{\partial \zeta} - \frac{\partial \hat{x}}{\partial \zeta} \frac{\partial z}{\partial \hat{\xi}}, \quad \frac{\partial \hat{x}}{\partial \hat{\eta}} \frac{\partial z}{\partial \hat{\xi}} - \frac{\partial \hat{x}}{\partial \hat{\xi}} \frac{\partial z}{\partial \hat{\eta}} \right) \rightarrow 0, \quad (5.5)$$

which is just (4.9) in terms of the computational variables $(\hat{\xi}, \hat{\eta}, \zeta)$, a singularity occurs in the boundary-layer solution. This must be the terminal point t_s in the numerical integrations in the Lagrangian coordinates; the time step Δt was gradually reduced as the calculations started to show clearly the evolution of such a stationary point. A stationary point can also develop on either of the symmetry planes at $z=0$ and 1 , as $(x_\xi, x_\eta) \rightarrow 0$ (see (4.20)); however, this situation did not occur in any of the cases considered. The evolution of a singularity was detected in the manner described in the Appendix.

6. Calculated results

Two types of three-dimensional boundary layers were considered corresponding to $\kappa > 0$ and $\kappa < 0$. For $\kappa > 0$, there is one parameter c associated with the inviscid flow (2.1) which is effectively an aspect ratio describing the streamwise length of the three-dimensional distortion relative to the spanwise spacing. In the limit $c \rightarrow 0$, the motion is two-dimensional and a singularity for the vortex of positive rotation occurs

c	t_f	t_0	t_s	x_s	z_s
0.05	0.744	0.6	0.94	0.14	0.59
0.1	0.723	0.6	0.82	0.13	0.54
0.2	0.584	0.5	0.61	0.16	0.55
0.5	0.281	0.24	0.28	0.30	0.58
1.0	0.133	0.11	0.13	0.42	0.61

TABLE 1. Calculated results for the vortex of positive rotation showing separation location (x_s, z_s) and separation time t_s ; t_f denotes failure time of the Eulerian computation and t_0 is the time when a switch to Lagrangian coordinates was made.

for $t_s \approx 0.989$ (Peridier *et al.* 1991). Increasing c gives rise to enhanced spanwise motion and this was generally found to hasten separation. Each calculation can require several weeks of computing time on a single-processor workstation, and most of the calculations were carried out on a Cray T3E using up to 64 processors. A number of meshes were used as a check on the accuracy and the results shown here are based on a mesh of $(301 \times 201 \times 201)$ in the (x, y, z) -directions, respectively. Preliminary calculations with mesh sizes twice as large were done to estimate a suitable switchover time (t_0) to the Lagrangian calculations, as well as to provide a check on the accuracy of the more refined calculations. A number of different time steps were also used as a check on the accuracy. During the course of a calculation, a very small time step (Δt) was used in the initial stages in Eulerian coordinates (typically $\Delta t = 0.0005$) because the initial variations with time are relatively large. After $t = 0.01$, the time step was then progressively increased to $\Delta t = 0.001$ and remained unchanged for most of the integration. Towards the end of a calculation near t_s , the time step was again reduced progressively from $\Delta t = 0.001$ to smaller values (typically in the range $0.0001 \leq \Delta t \leq 0.0005$). The singularity time t_s can be estimated from the time t_f at which the Eulerian calculation fails. The need for reduction of the time step to very small values as a Lagrangian calculation approaches t_s is because high accuracy is needed in the algorithm for locating the separation point (see the Appendix). A Lagrangian calculation can proceed without complication beyond the separation time and thus it is necessary to take small time steps near the end to determine a precise value of t_s .

6.1. The vortex of positive rotation

Calculations were carried out for $c = 0.05, 0.1, 0.2, 0.5$ and 1 to determine the effect of an increasing level of three-dimensional flow. The calculated separation times and locations for each case are listed in table 1. The separation process always develops at locations well above the surface. It may be noted that for the almost two-dimensional case $c = 0.05$, the separation time is close to the value $t_s = 0.989$ calculated by Peridier *et al.* (1991) and for an increasing level of three-dimensionality in the external flow, the separation time decreases.

The issue of what should be plotted to illustrate the unsteady flow development is a difficult one. On the symmetry planes, particle traces represent the instantaneous streamlines. On these planes, $w = 0$ and fluid particles cannot leave the plane except at isolated points. In figure 3, some typical results are shown for the almost two-dimensional case of $c = 0.05$. In each graph, there are two saddle points and one spiral node; the flow leaves the plane $z = 0$ at the node and moves toward the plane at $z = 1$; the flow enters $z = 1$ at the node. Note that the streamlines have developed

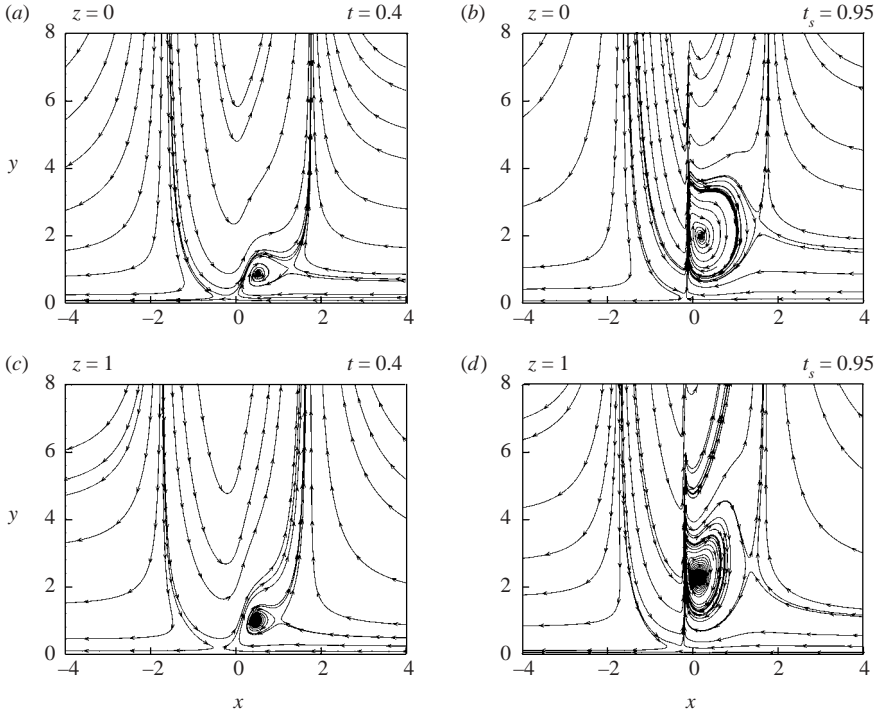


FIGURE 3. Instantaneous streamlines on the symmetry planes at selected times for $\kappa > 0$ and $c = 0.05$.

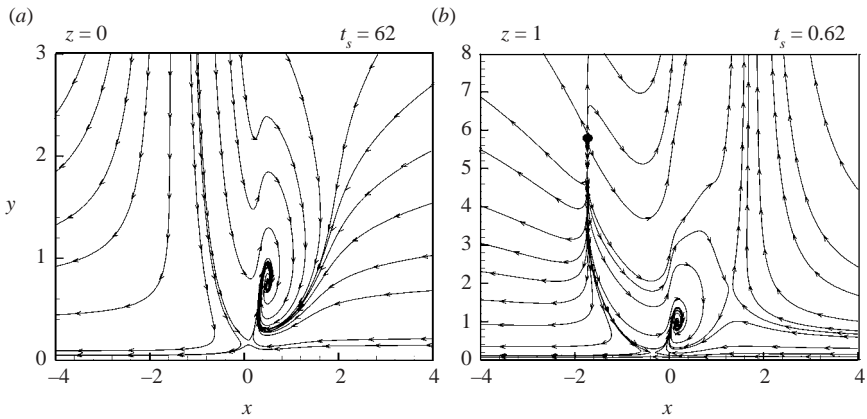


FIGURE 4. Instantaneous streamlines at the singularity time for $c = 0.2$ for (a) $z = 0$ and (b) $z = 1$ (the black dot indicates a node).

a prominent kink by $t = t_s$ on $z = 1$ in figure 3(d), while a similar but less developed behaviour occurs on $z = 0$ in figure 3(b). As indicated in table 1, separation occurs in the interior (and closer to the plane $z = 1$) where a sharp spike occurs in the instantaneous streamlines and the displacement thickness. The flow pattern developments on the symmetry planes are similar for the case $c = 0.1$, but begin to change somewhat for $c = 0.2$, as shown in figure 4 where instantaneous streamlines on the symmetry planes are shown at the singularity time. Again, a swirling focus develops on both

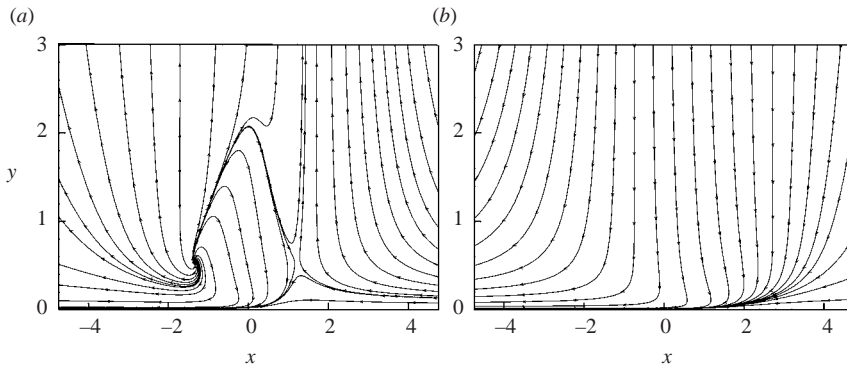


FIGURE 5. Instantaneous streamlines on the symmetry planes for $c=0.5$ for (a) $z=1$ and (b) $z=0$ at the singularity time $t_s=0.28$.

$z=0$ and 1, but in addition there is a nodal point which is not a focus on $z=1$. This feature is indicated as a large block dot; it occurs at an early stage in the computations near the wall and moves progressively away from the surface; here, the flow is directed into the plane $z=1$. At separation, there is no spiky behaviour in either plane. Finally, the case $c=1$ is considered in figure 5. At the singularity time, there is no indication of swirling motion on $z=0$. The focus on $z=1$ appears at a fairly early stage and by $t=0.13$ the spiralling motion has grown substantially in the normal direction. There is, however, no indication on either symmetry plane of the spiky behaviour that is occurring at this stage in the interior.

It is less clear how to illustrate the developing flow structure in the interior region $0 < z < 1$. Instantaneous three-dimensional streamlines can be easily plotted but appear as a 'spaghetti-like' entanglement which is almost impossible to interpret. An alternative, which is sometimes used in experimental flow visualization, is to consider the instantaneous velocity field in a plane. Some examples of this procedure applied to the present results for $c=0.5$ are shown in figure 6, where instantaneous streamlines of the in-plane velocity field are given in different planes (normal to the wall) between the symmetry planes. Clearly, there is a suggestion of apparent recirculating flow in some of these slices. However, the graphs are misleading to an extent since the spanwise velocity is non-zero at most points and so there is motion in and out of all of these planes. Apparent recirculation can also be seen in a variety of other planes for these flows, including some of those taken at constant x near $x=0$ and $x=1$. Various other sets of planes were considered in an attempt to discern the possible form of the flow structure that was developing under the influence of the external pressure gradient; these attempts were unsuccessful and in agreement with Dallmann (1988), it may be concluded that the usefulness of two-dimensional slices of these developing three-dimensional flows is questionable. It is of interest to note that in the latter stages of the calculations stagnation points develop. For the strongly three-dimensional flows, i.e. for $c=0.2, 0.5$ and 1.0, two stagnation points were observed to develop within the computational domain. For weakening three-dimensionality, i.e. for the cases $c=0.05, 0.1$ only one stagnation point appeared during the course of the integrations. As an example, critical points for the case $c=1.0$ at $t=t_s$ were located at $(-0.94, 0.30, 0.89)$ and $(0.68, 0.93, 0.64)$; while the single critical point for the case $c=0.1$ was at $(0.35, 2.5, 0.66)$. These stagnation points normally appear close to the symmetry plane $z=1$ and then move slowly into the domain and drift upward. For

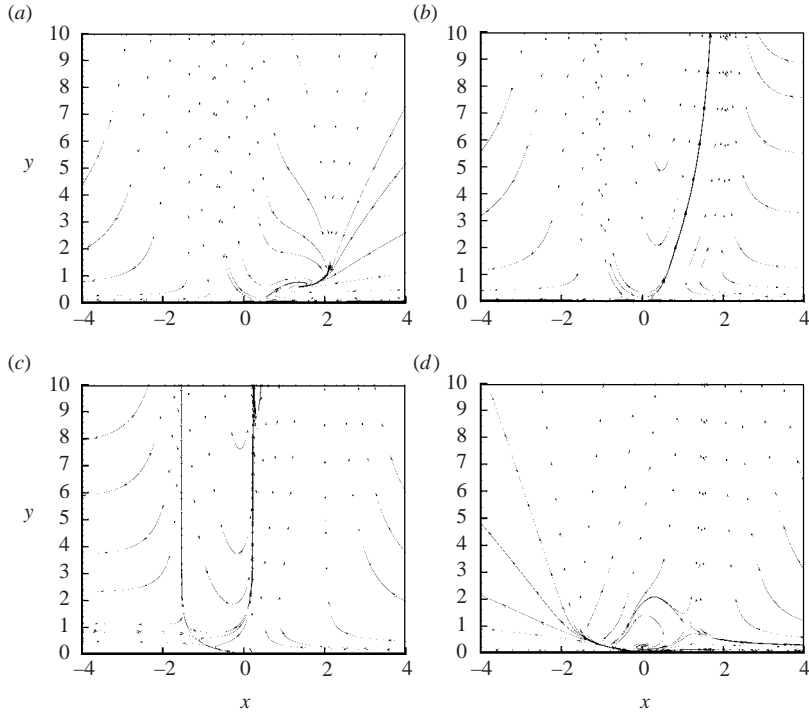


FIGURE 6. Instantaneous in-plane streamlines in various planes for $c=0.5$ at t_s for (a) $z=0.26$, (b) $z=0.393$, (c) $z=z_s=0.58$, (d) $z=0.793$.

example, for the case $c = 0.1$, the stagnation point is at $(0.48, 1.04, 0.81)$ when $t = 0.4$ and at $(0.36, 2.3, 0.67)$ when $t = 0.7$. Eventually, separation occurs in the vicinity of the stagnation points in all cases, but still an $O(1)$ distance away. These unsteady stagnation points do not seem to be useful in elucidating the possible unsteady flow structure and also do not appear to be associated with the eventual location of the separation point.

Another common means of characterizing three-dimensional flow is to consider the limiting streamlines on the surface. Near the surface in the laboratory frame of reference

$$u \approx -y\omega_z + \dots, \quad w \approx y\omega_x + \dots, \quad (6.1)$$

where the vorticity components are defined by

$$\omega_x = \frac{\partial w}{\partial y}, \quad \omega_z = -\frac{\partial u}{\partial y}, \quad (6.2)$$

and in (6.1), ω_x and ω_z are evaluated on the wall at $y=0$. The limiting streamlines and vortex lines on the surface through any point on the surface are evaluated by integration of the equations

$$\frac{dz}{dx} = -\frac{\omega_x}{\omega_z} \Big|_{y=0}, \quad \frac{dz}{dx} = \frac{\omega_z}{\omega_x} \Big|_{y=0}, \quad (6.3)$$

respectively, through various points in the (x, z) -plane. Both sets of trajectories are orthogonal and are shown in figure 7 at the singularity time t_s for representative cases of $c = 0.1$ and $c = 0.5$. On these plots, there is a node and a saddle point, each of which

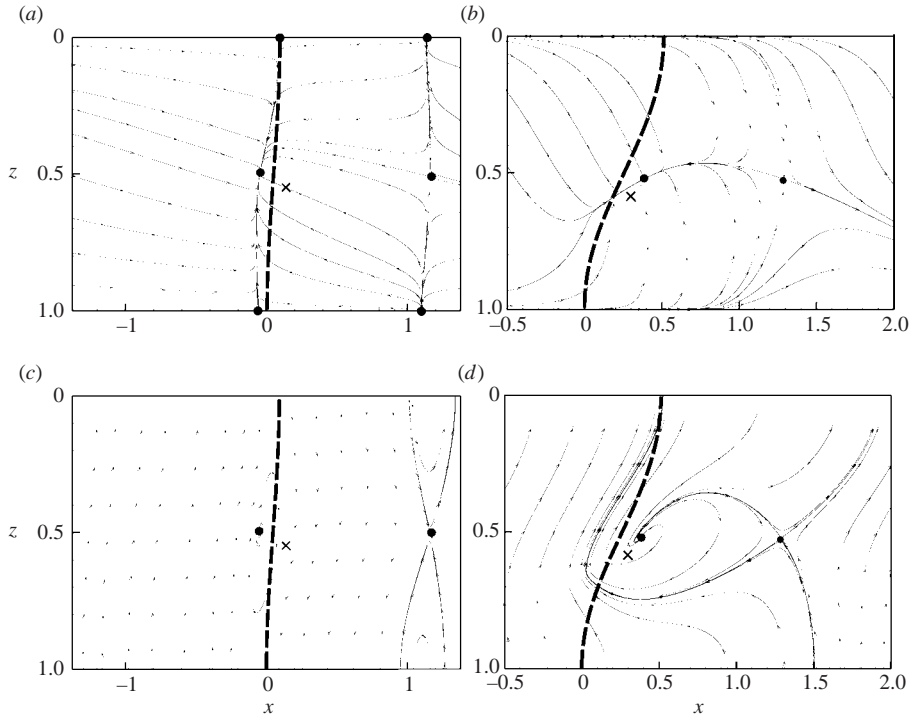


FIGURE 7. Limiting streamlines and vortex lines on the wall at separation for $c=0.1$ (a) streamlines, (c) vortex lines and $c=0.5$, (b) streamlines and (d) vortex lines.

is denoted by a black circle. These critical points generally appeared simultaneously at an earlier time in the calculation. The general change in topology from the almost two-dimensional case $c=0.1$ to a strongly three-dimensional flow for $c=0.5$ is suggested in these plots. For $c=0.5$, the node and the saddle point are ultimately connected directly by a limiting streamline (often referred to as a line of separation; see, for example Tobak & Peake 1982). It may be noted that it is well-known from the two-dimensional case that the ‘line of separation’ in the wall shear is fundamentally not the same as the actual separation position, even though they are usually relatively close to one another. In each of these plots, the projection of the vortex core in the inviscid flow above (i.e. $x = f(z)$) is shown as a broken line and the projection of the actual separation point is shown as a cross. Since unsteady separation is a phenomenon which generally develops above the wall (Van Dommelen & Cowley 1990), it is not surprising that neither the limiting streamlines nor the wall vortex lines are useful in determining the eventual location of separation or the occurrence of the separation event that has developed aloft. Note that the surface streamlines and vortex lines exhibit regular behaviour even at separation, as originally noted by Van Dommelen & Cowley (1990).

Although the appearance of swirling motion in some planes seems to be an indicator that a separation event may occur at a subsequent time, this type of criterion is poorly defined and in some situations is not reliable. The best indication that separation is imminent may be observed by plotting the surfaces $\omega_x = 0$ and $\omega_z = 0$. When these surfaces intersect they do so in a three-dimensional space curve C , in general, and when this happens a crisis situation exists for the boundary layer since now there is a line of

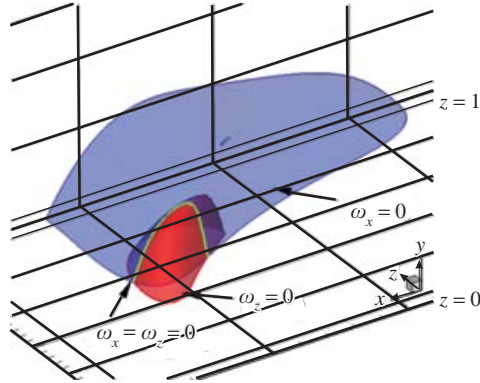


FIGURE 8. Intersecting surfaces of zero vorticity components; the line where both ω_x and ω_z are zero is also shown for the case $c = 1$, $t = 0.12 < t_s$.

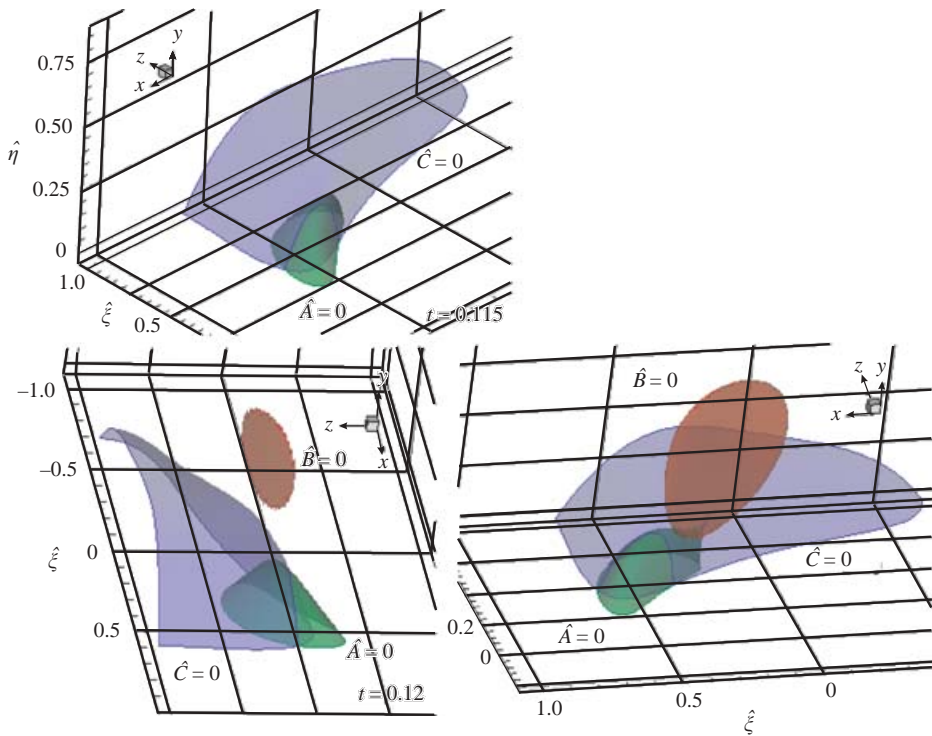


FIGURE 9. Contour surfaces of $\hat{A} = 0$, $\hat{B} = 0$ and $\hat{C} = 0$ at (a) $t = 0.115$, (b) $t = 0.12$, (c) $t_s = 0.13$. Notice that surface $\hat{B} = 0$ has not yet appeared at $t = 0.115$. All three surfaces touch at a single location $(\hat{\xi}_s, \hat{\eta}_s, \hat{\zeta}_s)$ at $t_s = 0.13$.

fluid particles for which both vorticity components are zero. It is somewhere along this curve C where a fluid particle is eventually compressed to zero thickness at separation. A typical situation observed in the present calculations is shown in figure 8 for $c = 1.0$ at $t = 0.12$ (which is in advance of separation time $t_s = 0.13$). Note that the surface $\omega_x = 0$ extends through the symmetry plane $z = 1$ to the region $z > 1$; this surface appears at an early stage in the calculations and expands mainly in the x -direction. The surface $\omega_z = 0$ appears at a later stage immediately intersecting the surface

$\omega_x = 0$. The surface $\omega_z = 0$ then expands in both directions with time. The reason that the intersection is an important event can be understood by extension of an argument due to Van Dommelen (1991) for two-dimensional flows.

At the initiation of the motion, ω_x is everywhere positive and ω_z is everywhere negative in the boundary layer. At the wall, it follows from equations (3.1a) and (3.1b) that the surface vorticity fluxes are

$$q_{w_x} = -\left. \frac{\partial \omega_x}{\partial y} \right|_{y=0} = -\frac{\partial p_\infty}{\partial z}, \quad q_{w_z} = -\left. \frac{\partial \omega_z}{\partial y} \right|_{y=0} = \frac{\partial p_\infty}{\partial x}, \quad (6.4)$$

where $p_\infty(x, z)$ denotes the (steady) external pressure field. In regions where p_∞ increases in the spanwise direction, eventually a volume where $\omega_x < 0$ will diffuse from the wall into the region above where $\omega_x > 0$. Similarly, in portions of the (x, z) -plane where the streamwise pressure gradient is increasing in x , a volume of positive ω_z eventually penetrates into the zone where $\omega_z < 0$ above. The two surfaces $\omega_x = 0$ and $\omega_z = 0$ define the outlines of these two volumes and when the surfaces intersect in a space curve C , a separation event is expected at finite time. Since both vorticity components are zero there, the curve C will be referred to as the zero vorticity line. With the passage of time, the zero vorticity line will be convected into the outer regions of the boundary layer where the flow processes are essentially inviscid; the vorticity is constant along C and the majority of C (at locations away from the surface) is now a material line. At this stage, the pressure field (which initiated the sequence) and the viscous terms fade in importance and convection becomes dominant. Then, along C the momentum equations (3.1a) and (3.1b) become

$$\frac{\partial u}{\partial t} + u \frac{\partial u}{\partial x} + w \frac{\partial u}{\partial z} \approx 0, \quad \frac{\partial w}{\partial t} + u \frac{\partial w}{\partial x} + w \frac{\partial w}{\partial z} \approx 0. \quad (6.5a, b)$$

As noted by Van Dommelen (1991), (6.5a) for two-dimensional flow ($w = 0$) is known as Burgers' equation, which is often used to model shock formation in unsteady one-dimensional gas dynamics. Because the majority of C is a material line, fluid particles along C are trapped there; however, according to (6.5), the velocity components of each particle along C are conserved. Under certain conditions on the sign of various derivatives, it can be shown that a particle collision on C will occur and a fluid particle at separation is eventually compressed to zero thickness. A referee has suggested that the collision is not normally in the direction of the curve C , but in a direction oblique to it, as a particle on C collides with a particle immediately next to it. In any event, it was verified that separation took place on C in all the present results. Since the compressed particle cannot lengthen toward the wall, it must do so toward the mainstream in what appears to be a needle-like spiky eruption. It is this complex behaviour at separation which necessitates a prior switch to the Lagrangian formulation.

The issue of how to determine when a separation event occurs is now taken up. The condition (4.10) given by Van Dommelen & Cowley (1990) describes the requirement for the evolution of a singularity in the continuity equation. This condition, however, is difficult to detect in a computational scheme since it need not occur exactly at a mesh point. Here, an alternative approach was developed using conditions (5.5) and the results developed in the Appendix. In computational variables, the conditions for a stationary point are given by $\hat{A} = \hat{B} = \hat{C} = 0$ at t_s in Lagrangian coordinates, where \hat{A} , \hat{B} and \hat{C} are defined in the Appendix. The three surfaces \hat{A} , \hat{B} and \hat{C} are related to the vorticity components $\omega_x = -\partial u / \partial y$ and $\omega_z = \partial w / \partial y$. In terms of the

computational Lagrangian variables

$$\omega_z = -\Omega \left[\hat{A} \frac{\partial}{\partial \hat{\xi}} + \hat{B} \frac{\partial}{\partial \hat{\eta}} + \hat{C} \frac{\partial}{\partial \hat{\zeta}} \right] u, \quad \omega_x = \Omega \left[\hat{A} \frac{\partial}{\partial \hat{\xi}} + \hat{B} \frac{\partial}{\partial \hat{\eta}} + \hat{C} \frac{\partial}{\partial \hat{\zeta}} \right] w, \quad (6.6a)$$

where

$$\Omega = \frac{2}{\pi c_y} \left\{ \frac{\cos(\frac{1}{2}\pi\hat{\xi}) \cos(\frac{1}{2}\pi\hat{\eta})}{\cos(\frac{1}{2}\pi\hat{x})} \right\}^2. \quad (6.6b)$$

It follows that when $\hat{A} = \hat{B} = \hat{C} = 0$, both vorticity components are simultaneously zero.

Figure 9 illustrates the three surfaces $\hat{A} = 0$, $\hat{B} = 0$ and $\hat{C} = 0$ in varying perspectives at $t = 0.115, 0.12$ and $t_s = 0.13$ in three-dimensional computational space $(\hat{\xi}, \hat{\eta}, \hat{\zeta})$. For this particular case, the switchover from Eulerian to Lagrangian calculations was done at $t = 0.11$. The surfaces $\hat{A} = 0$ and $\hat{C} = 0$ are present at $t = 0.115$ and grow rapidly in the normal direction; the surface $\hat{B} = 0$ is not yet present. The surface $\hat{B} = 0$ has a thin oval shape and eventually appears aloft from the wall; it grows in the normal direction but never touches the wall, unlike the other two surfaces that appear at the wall surface initially and then grow outward. The surfaces $\hat{A} = 0$ and $\hat{B} = 0$ exhibit similar behaviour to the contours $-\partial\hat{x}/\partial\hat{\eta} = 0$ and $\partial\hat{x}/\partial\hat{\xi} = 0$ in two-dimensional separation problems, where the contour $\partial\hat{x}/\partial\hat{\eta} = 0$ appears attached to the wall and the contour $\partial\hat{x}/\partial\hat{\xi} = 0$ appears aloft (see, for example Degani *et al.* 1998). The three surfaces $\hat{A} = 0$, $\hat{B} = 0$ and $\hat{C} = 0$ grow in size with time and eventually intersect one another at a point denoted by $\hat{\xi}_s, \hat{\eta}_s, \hat{\zeta}_s$ at t_s , as shown in figure 9(c). Once the instant (t_s) and the local position $(\hat{\xi}_s, \hat{\eta}_s, \hat{\zeta}_s)$ where all the three surfaces vanish simultaneously was located, a singularity had been detected and the Lagrangian calculation was terminated (see the Appendix).

Boundary-layer growth can be observed through the temporal development of the displacement thickness. There are two components of displacement thickness in three dimensions, i.e. $\delta_x^*(x, z, t)$ and $\delta_z^*(x, z, t)$, defined here in terms of the velocities in the laboratory frame of reference by

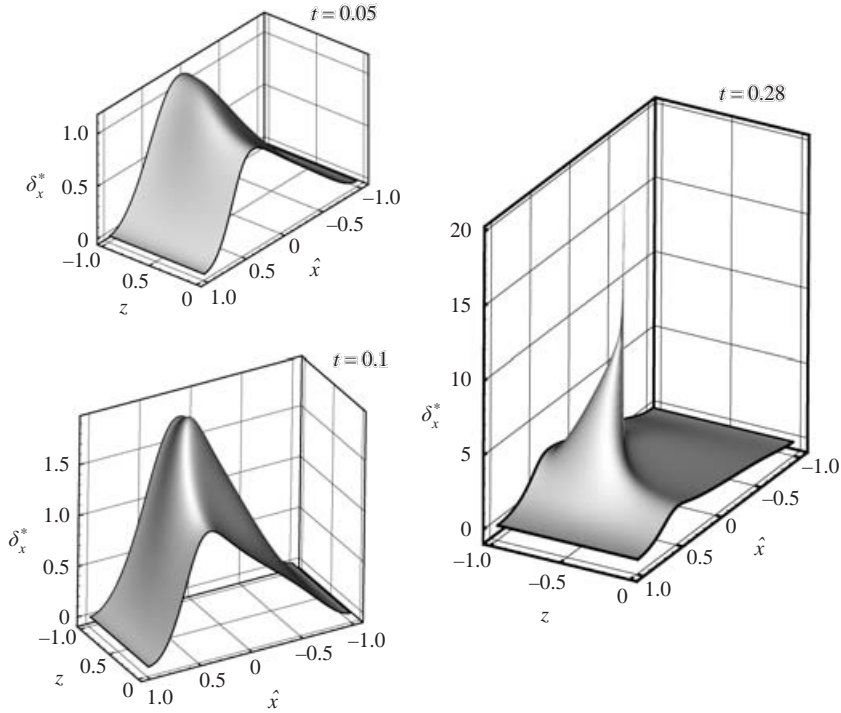
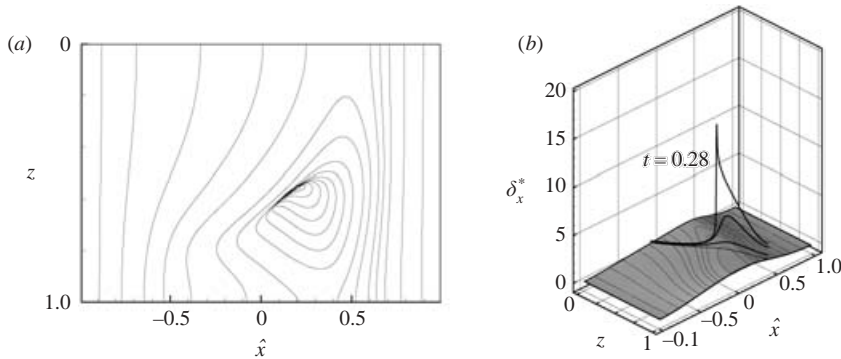
$$\delta_x^* = \int_0^\infty \left(1 - \frac{u_l}{U_{\infty,l}} \right) dy, \quad \delta_z^* = \int_0^\infty \left(1 - \frac{w_l}{W_{\infty,l}} \right) dy, \quad (6.7)$$

where the subscript l denotes the laboratory frame of reference. For the vortex with positive rotation ($\kappa > 0$), it is possible to use normalized velocities U and W in both Eulerian and Lagrangian calculations and the velocities in the laboratory frame are $u_l = u + 1 = UU_e$ and $U_{\infty,l} = U_\infty + 1 = U_e$ for the streamwise velocity and $w_l = WW_e$ and $W_{\infty,l} = W_e$ for the spanwise velocity. Thus, (6.7) becomes

$$\delta_x^* = \int_0^\infty (1 - U) dy, \quad \delta_z^* = \int_0^\infty (1 - W) dy. \quad (6.8)$$

For the Lagrangian calculations, δ_x^* and δ_z^* in (6.8) were evaluated by solving the continuity equation along each characteristic curve from the wall in the computational domain (\hat{x}, z) (see the Appendix).

The temporal development of δ_x^* is illustrated in figure 10 in computational coordinates. As the boundary layer responds to the external pressure gradients, δ_x^* develops a rising ridge which is highest in the middle of the span near where the singularity eventually occurs at t_s ; the behaviour of δ_z^* is similar, but is not shown here. Explosive boundary-layer growth finally occurs as $t \rightarrow t_s = 0.28$ and at $x_s = 0.30$,


 FIGURE 10. Temporal development of the displacement thickness δ_x^* for $c = 0.5$.

 FIGURE 11. (a) level contours of δ_x^* at separation for $c = 0.5$ and (b) temporal development of δ_x^* in the q -plane ($t = 0.05, 0.1, 0.2, 0.28$).

$z_s = 0.58$ and is shown in the last plot of figure 10. This is the behaviour described on a theoretical basis by Van Dommelen & Cowley (1990). The level contours of δ_x^* at separation are shown in figure 11. An abrupt and substantial increase of the displacement thickness along a narrow ridge between $t = 0.2$ and $t_s = 0.28$ may be observed in figure 11(b) over a very narrow streamwise range. The plotted development is in a plane that will be described as the q -plane. This plane is oriented normal to the wall and in the q -direction defined in connection with (4.10). The q -plane slices the eruptive ridge shown in figure 10(c) in a direction normal to the ridge. In the q -plane, the separation event appears similar to that in two dimensions (see, for example

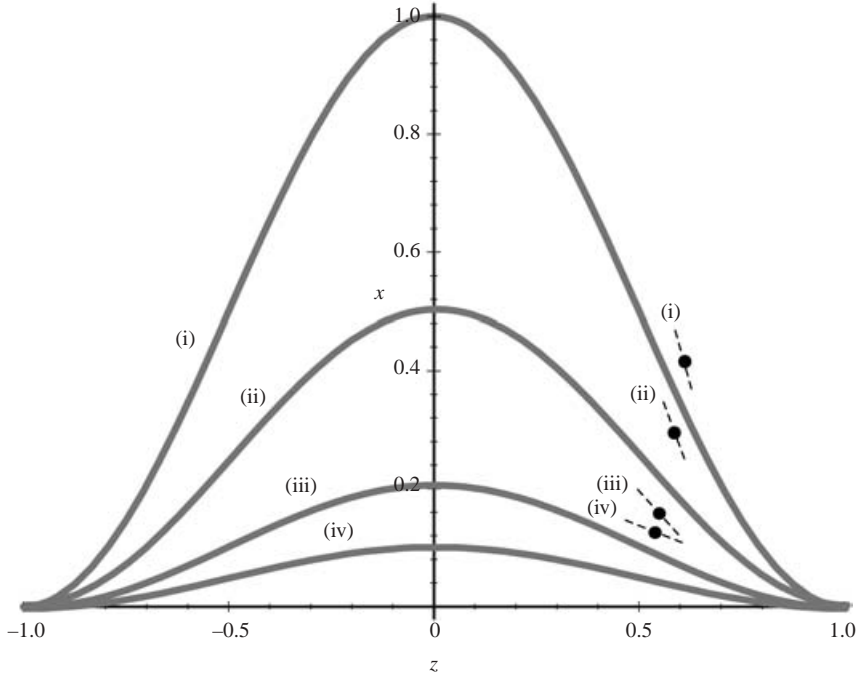


FIGURE 12. Projection of vortex core (i.e. $f(z)$) in the (x, z) -plane showing separation locations for (i) $c = 1$, (ii) $c = 0.5$, (iii) $c = 0.2$, (iv) $c = 0.1$ for $\kappa > 0$.

Peridier *et al.* 1991) as predicted by Van Dommelen & Cowley (1990). Lastly, in figure 12, the location of separation in the (x, z) -plane is shown for the four different cases. The separation location is shown as a small black circle and the small broken lines are the q_n -direction defined previously (as normal to the q -direction); the broken lines thus indicate the longitudinal orientation of the erupting tongue at separation. It is evident that with increasing three-dimensionality, the separation event occurs closer to the vortex core and along a ridge that is closer to being parallel to the local axis of the vortex (i.e. $x = f(z)$).

In the theoretical structure described by Van Dommelen & Cowley (1990), the displacement surfaces near separation should thicken proportional to $(t - t_s)^{-1/4}$ as $t \rightarrow t_s$ and thin proportional to $(t - t_s)^{3/2}$ and $(t - t_s)^{1/2}$ in the q - and q_n -directions, respectively. The q_n -direction can be seen easily from the contour plots of δ_x^* as seen in figure 11(a); at separation, the contour lines of δ_x^* are parallel and very close to one another and a line parallel to these lines defines the q_n -direction. The q -direction is perpendicular to the q_n -direction. The q -direction was also evaluated by confirming that at separation there is a constant λ such that (4.10) is satisfied. To confirm the behaviour predicted by Van Dommelen & Cowley (1990), contours of the maximum displacement thickness were plotted at a sequence of times just prior to a separation event. These contours are closed curves and the thickness of the contour in the q - and q_n -directions was estimated at each time. The growth in δ_x^* was consistently observed to behave according to $(t_s - t)^{-1/4}$ and, for example, for $c = 0.5$ it was found that $\delta_x^* \approx 2.9 \times (t_s - t)^{-1/4}$. Similarly, the thinning in the q - and q_n -directions was broadly consistent with the scalings predicted by Van Dommelen & Cowley (1990) and for $c = 0.5$, the thinning in the q - and q_n -directions was observed to behave as $1.5 \times 10^3 (t_s - t)^{3/2}$ and $49 \times (t_s - t)^{1/2}$. These estimates of the boundary-layer growth

were obtained by least-squares curve fits to the numerical data and the exponents were consistently found to be within 1% of the values quoted here. Note, however, that the surface near the sharp tip has almost zero thickness and is very difficult to resolve accurately.

Near the location of the maximum displacement thickness at $t = t_s$, the contour lines in (\hat{x}, z) shrink to a very thin region (see figure 11a). The difference from two-dimensional flows is that the spike occurs at a point (as opposed to a knife edge in two dimensions) and the ridge falls away to either side in the q_n -direction. One problem associated with this erupting tongue is that it was essentially impossible to compute a smooth surface near the tip. Points on the surfaces for δ_x^* and δ_z^* are obtained by the numerical integration method described in the Appendix along characteristic curves that originate on the wall. A characteristic from some location on the wall tracks upward to the boundary-layer edge and the values obtained define a point on the surfaces for δ_x^* and δ_z^* . Because the surface near the tip of the tongue has almost zero thickness and is sharply rising, it proves very difficult to adjust the starting locations of the characteristic integrations to define precisely the upper extremities of the tongue. For this reason, the definition of the tip of the tongue tends to be somewhat ragged, as may be confirmed upon very close examination of figure 10.

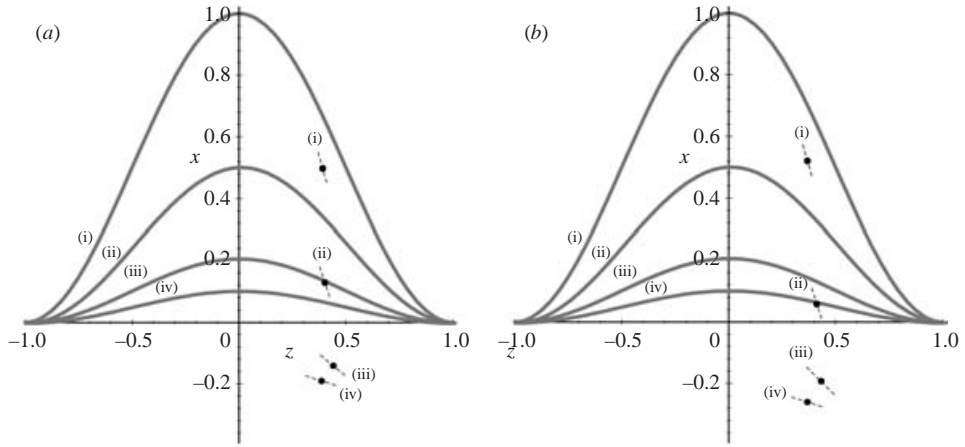
6.2. The vortex of negative rotation

This case mimics a vortex of negative rotation ($\kappa < 0$) convecting in a uniform flow above a wall and models the motion at the wall induced by a convected hairpin vortex. In a frame of reference moving with the vortex, $u = -\beta$ at $y = 0$ (i.e. the wall moves uniformly to the left with speed $-\beta$); here, β is related to the fractional convection rate α of the vortex by $\beta = \alpha/(1 - \alpha)$ for a two-dimensional vortex (Doligalski & Walker 1984). The range of interest is $0 \leq \alpha \leq 1$ (or $0 \leq \beta \leq \infty$) as described in §2.2, but only two sets of results will be described here corresponding to $\beta = 0.2$ and $\beta = 0.5$. The case $\beta = 0.2$ may be viewed as a strong vortex moving at about $\alpha = 1/6$ of uniform flow speed in which it is embedded. The case $\beta = 0.5$ can be regarded as a somewhat weaker vortex moving at $\alpha = 1/3$ of the uniform flow speed. Both values of α are well below the critical value $\alpha_c = 0.58$ for which separation is suppressed in a two-dimensional flow by the influence of the moving wall and thus separation is expected here in both sets of results. The inviscid surface streamlines are as shown in figure 2 (the flow direction is reversed from the previous cases of $\kappa > 0$).

As in the case of $\kappa > 0$, the solutions for $\kappa < 0$ were computed with at least two sets of mesh sizes and several time steps as a check on the accuracy. Calculated results are given in table 2 for the position and time of separation. Note that the faster moving vortex generally produces separation at a later time for the almost two-dimensional cases (e.g. $c = 0.1$). In such cases, the adverse streamwise pressure gradient is dominant and the moving wall below exerts a significant influence in delaying separation. With increasing c , the spanwise adverse pressure gradient becomes progressively more dominant and separation times and locations become comparable for each value of c . In all cases, separation now occurs behind the vortex core as shown in figure 13.

As in the case of $\kappa > 0$, the instantaneous streamline patterns on the symmetry plane for the almost two-dimensional cases, show similar development to the corresponding two-dimensional solutions of Doligalski & Walker (1984). Some typical results for $c = 0.1$ and $\beta = 0.2$ are shown in figure 14, where it may be noted that the streamlines

c	β	x_s	z_s	t_s
0.1	0.2	-0.19	0.39	0.67
	0.5	-0.26	0.37	0.69
0.2	0.2	-0.14	0.44	0.57
	0.5	-0.19	0.43	0.57
0.5	0.2	0.13	0.40	0.28
	0.5	0.06	0.41	0.28
1.0	0.2	0.50	0.39	0.13
	0.5	0.52	0.38	0.13

TABLE 2. Calculated results for $\kappa < 0$.FIGURE 13. Projection on (x, z) -plane of the vortex core for (a) $\beta = 0.2$ and (b) $\beta = 0.5$ showing the separation location and the q_n -direction for (i) $c = 1.0$, (ii) $c = 0.5$, (iii) $c = 0.2$, (iv) $c = 0.1$.

on both planes are developing a spiky behaviour at $t = t_s$. However, as indicated in figure 13, separation actually occurs in the interior $0 < z < 1$. The symmetry planes are not, however, a reliable indicator of developing structure in the interior. In fact, for many cases at larger values of c , there is no evidence of recirculation on the symmetry planes at separation. Again the reliable precursor of separation is the intersection of the two zero vorticity surfaces $\omega_x = 0$, $\omega_z = 0$.

For the negative rotation vortex, the conventional displacement thicknesses δ_x^* and δ_z^* given by (6.8) cannot be defined. Considering the velocity components in the boundary layer to be expressed in terms of functions ψ and ϕ according to (A 5), it may be inferred that

$$\psi \sim yU_\infty(x, z) - \tilde{\delta}_x^*(x, z, t), \quad \phi \sim yW_\infty(x, z) - \tilde{\delta}_z^*(x, z, t) \quad (6.9)$$

at the boundary-layer edge, where $\tilde{\delta}_x^*$ and $\tilde{\delta}_z^*$ are functions defined by

$$\tilde{\delta}_x^* = \int_0^\infty (U_\infty - u) dy, \quad \tilde{\delta}_z^* = \int_0^\infty (W_\infty - w) dy. \quad (6.10)$$

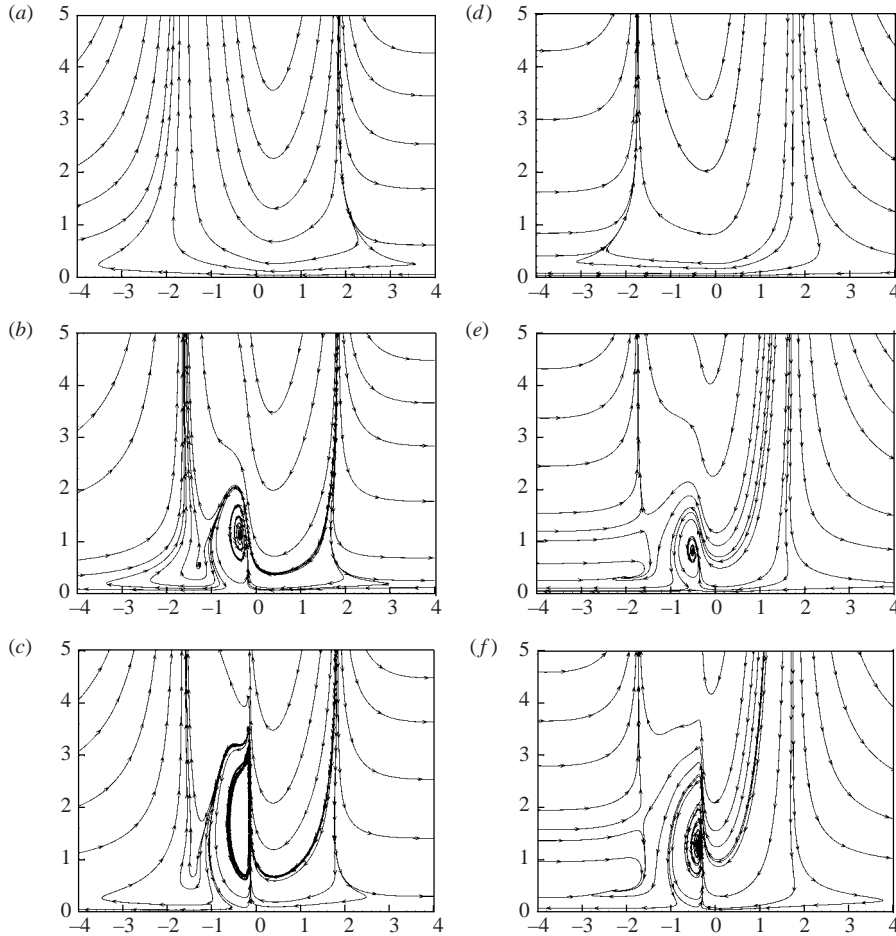


FIGURE 14. The instantaneous streamlines on the symmetry plane for $c=0.1$ and $\beta=0.2$; $z=0$ for (a) $t=0.1$, (b) $t=0.5$, (c) $t_s=0.67$ and $z=1$ for (d) $t=0.1$, (e) $t=0.5$, (f) $t_s=0.67$.

In addition, at the boundary-layer edge

$$v \sim - \left(\frac{\partial U_\infty}{\partial x} + \frac{\partial W_\infty}{\partial z} \right) y + \left(\frac{\partial \tilde{\delta}_x^*}{\partial x} + \frac{\partial \tilde{\delta}_z^*}{\partial z} \right). \quad (6.11)$$

The first term on the right-hand side of (6.11) is necessary to effect the matching to the external flow, while the second is associated with the vertical velocity at the boundary-layer edge induced by events taking place in the boundary layer. In Lagrangian coordinates, the perturbation functions $\tilde{\delta}_x^*$ and $\tilde{\delta}_z^*$ can be computed at any instant along the characteristics.

The development of boundary-layer growth is illustrated in figure 15. A large negative spike is observed to develop in the middle of the domain at $(\hat{x}_s, z_s) = (0.13, 0.40)$, where the singular nature of the solution at $t_s = 0.28$ can be clearly seen in the side view of $\tilde{\delta}_x^*$. Similar behaviour was also observed for $\tilde{\delta}_z^*$. It may be inferred from (6.11) that this behaviour in $\tilde{\delta}_x^*$ and $\tilde{\delta}_z^*$ implies sharp focused outflow from the boundary

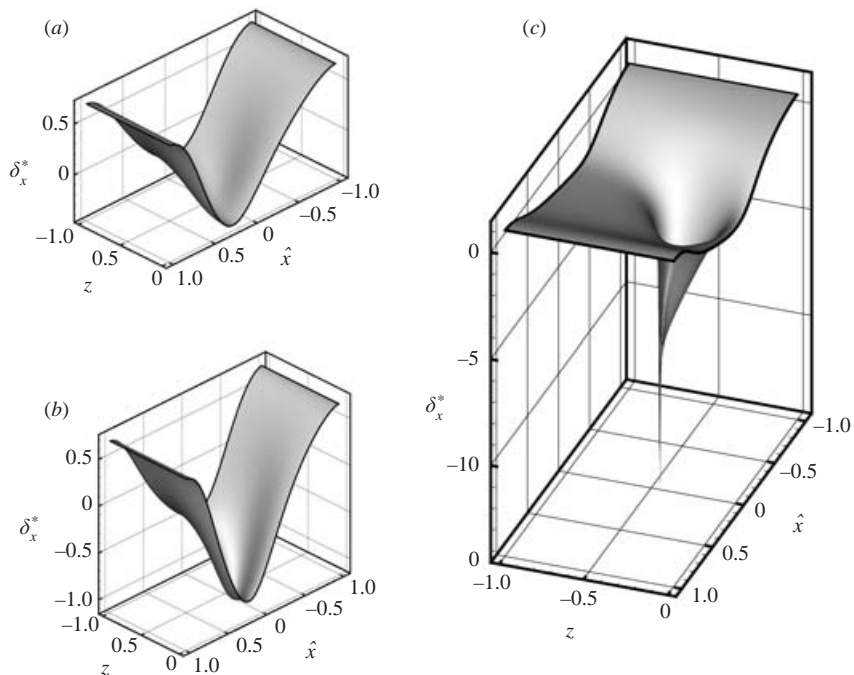


FIGURE 15. The temporal development of the function $\tilde{\delta}_x^*$ for $c = 0.5$.
(a) $t = 0.05$, (b) 0.10 , (c) 0.28 .

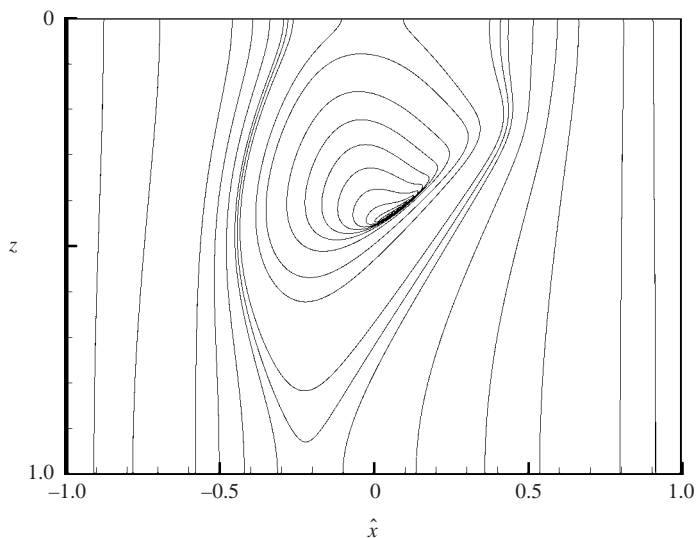


FIGURE 16. The level curves for $\tilde{\delta}_x^*$ in the (x, z) -plane at separation for $c = 0.5$.

layer; the spiky peaks of $\tilde{\delta}_x^*$ and $\tilde{\delta}_z^*$ occur in a narrow region where the streamlines become significantly squeezed and spiky at $t_s = 0.28$. Again the level contours shown in figure 16 of $\tilde{\delta}_x^*$ (or $\tilde{\delta}_z^*$) reveal the q - and q_n -directions.

7. Conclusions

Numerical solutions have been obtained for the unsteady boundary layer induced by an external mainstream flow that mimics a three-dimensional vortex of negative and positive rotation, respectively, above an infinite wall. It has been shown that the solution develops a separation singularity at a point in the (x, z) -plane and above the wall. At separation, the boundary-layer flow focuses into a sharply eruptive spike at a single point located on a ridge which generally lies at an angle to the x -axis; the results imply a sharp focused outflow from the boundary layer at that location. The characteristic feature of the development of the three-dimensional boundary-layer flow toward separation is similar to that observed in two dimensions previously by Van Dommelen & Shen (1980, 1982), Peridier *et al.* (1991) and Degani *et al.* (1998) and is entirely consistent with the theoretical predictions of Van Dommelen & Cowley (1990) and Van Dommelen (1991). Conclusions of the study are as follows:

(i) For a vortex of either positive or negative rotation, increasing the strength of the external cross-flow hastened separation.

(ii) For the vortex of negative rotation, separation was delayed as the convection speed of the vortex increased for small values of c , in agreement of the previous two-dimensional studies of Doligalski & Walker (1984) and Degani *et al.* (1998); for larger values of c the spanwise pressure gradient appears to be the dominant factor in inducing separation.

(iii) The intersection of the zero vorticity surfaces is the most reliable indication that a separation event is about to occur. Two-dimensional slices of the developing flow do not appear to be a useful diagnostic tool.

Finally, the calculated results tend to support the conjectures of Smith *et al.* (1991) and Smith & Walker (1997) concerning the process of how hairpin vortices can be regenerated in a turbulent boundary layer. Here, it has been demonstrated how a moving three-dimensional disturbance can provoke the occurrence of a sharply focused thin eruptive tongue of fluid at separation. As this tongue penetrates toward the outer inviscid flow region, an inviscid–viscous interaction will occur and the most likely outcome of this interaction is a roll-up into a hairpin vortex. However, it must be noted that theoretical descriptions of the unsteady viscous–inviscid interaction process are complex (see, for example, Hoyle & Smith 1994; Li *et al.* 1998; Smith, Bowles & Walker 2000) and the development of numerical algorithms that are capable of computing such an interaction is, at this stage, a remote event in the future (Walker 2003).

This work was supported by the Army Research Office under grant number 40019-DAAD19-99-1-0244. The research was supported in part by grant number CTS010001 from the Pittsburg Supercomputing Center, supported by several federal agencies, the Commonwealth of Pennsylvania and private industry. The authors would like to thank Professor L. L. Van Dommelen for helpful suggestions and the referees for their useful comments.

Appendix. Solution of the continuity equation

In order to view the Lagrangian results in the conventional Eulerian description of the flow field, it is necessary to solve for y and v at any time step, as well as to determine if a singularity has evolved. In computational coordinates $(\hat{\xi}, \hat{\eta}, \zeta)$, the continuity equation (4.3) becomes

$$\hat{A}\hat{y}_{\hat{\xi}} + \hat{B}\hat{y}_{\hat{\eta}} + \hat{C}\hat{y}_{\zeta} = \hat{D}, \quad (\text{A } 1)$$

where

$$\hat{A} = \frac{\partial \hat{x}}{\partial \zeta} \frac{\partial z}{\partial \hat{\eta}} - \frac{\partial \hat{x}}{\partial \hat{\eta}} \frac{\partial z}{\partial \zeta}, \quad \hat{B} = \frac{\partial \hat{x}}{\partial \hat{\xi}} \frac{\partial z}{\partial \zeta} - \frac{\partial \hat{x}}{\partial \zeta} \frac{\partial z}{\partial \hat{\xi}}, \quad (\text{A } 2a)$$

$$\hat{C} = \frac{\partial \hat{x}}{\partial \hat{\eta}} \frac{\partial z}{\partial \hat{\xi}} - \frac{\partial \hat{x}}{\partial \hat{\xi}} \frac{\partial z}{\partial \hat{\eta}}, \quad \hat{D} = \left\{ \frac{\cos(\pi \hat{x}/2) \cos(\pi \hat{y}/2)}{\cos(\pi \hat{\xi}/2) \cos(\pi \hat{\eta}/2)} \right\}^2, \quad (\text{A } 2b)$$

which is a first-order equation for \hat{y} . Here, $\hat{x}(\hat{\xi}, \hat{\eta}, \zeta, t)$ and $z(\hat{\xi}, \hat{\eta}, \zeta, t)$ are known at any instant t from a numerical solution of the Lagrangian boundary-layer equations given in §4. The characteristics are curves of \hat{x} and z constant, and the subsidiary equations are

$$\frac{d\hat{\xi}}{\hat{A}} = \frac{d\hat{\eta}}{\hat{B}} = \frac{d\zeta}{\hat{C}} = \frac{d\hat{y}}{\hat{D}} = d\hat{s}, \quad (\text{A } 3)$$

where \hat{s} is a parameter denoting distance along the characteristics. A numerical integration of (A 3) for \hat{y} is initiated at positions of $\hat{\xi}$ and ζ on the wall at $\hat{\eta} = \hat{y} = 0$ in the mesh. For a specific fluid particle on the wall (i.e. at specified values of $\hat{\xi}$ and ζ), the corresponding values of x and z are calculated from (4.6) in terms of the computational variables defined by (4.22), where $\beta = 1$ for $\kappa > 0$ and is a specified value for $\kappa < 0$.

Consider a specific location on the wall at $\hat{\xi} = \hat{\xi}_0$ and $\zeta = \zeta_0$ which may or may not be in the Lagrangian mesh. If the point is not in the mesh, bilinear interpolation can be used to obtain the values of $\hat{x}(\hat{\xi}, \hat{\eta}, \zeta, t)$ and $z(\hat{\xi}, \hat{\eta}, \zeta, t)$ at that point, since \hat{x} and z are known at the four neighbouring mesh points on the wall. The integration of (A 3) is advanced along the characteristics starting from the initial locations on the wall

$$\hat{\xi} = \hat{\xi}_0, \quad \zeta = \zeta_0, \quad \hat{\eta} = \hat{y} = 0 \quad \text{at } \hat{s} = 0, \quad (\text{A } 4)$$

using a straightforward generalization of a second-order accurate predictor–corrector algorithm described by Peridier *et al.* (1991; see also Degani *et al.* 1998), which generates points along the characteristics and the corresponding values of \hat{y} . The step size $\Delta \hat{s}$ in the numerical algorithm is generally chosen small enough so that iteration of the corrector formula is not necessary. Since points thus generated along the characteristic curves do not coincide with the mesh grid points, a three-dimensional linear interpolation (using neighbouring eight mesh points) was used to calculate the required values of \hat{A} , \hat{B} , \hat{C} and \hat{D} at any stage (Kim 1999).

The normal velocity v can be computed by introducing the intermediate functions $\psi(x, y, z, t)$ and $\phi(x, y, z, t)$ defined by

$$u = \frac{\partial \psi}{\partial y}, \quad v = -\frac{\partial \psi}{\partial x} - \frac{\partial \phi}{\partial z}, \quad w = \frac{\partial \phi}{\partial y}, \quad (\text{A } 5a-c)$$

in order to satisfy the continuity equation (3.1c); ψ and ϕ can be evaluated in the computational coordinates along the characteristic curves in a step-by-step manner. Then, v may be obtained from (A 5b), once ψ and ϕ are defined at each point in a three-dimensional mesh.

The same argument and procedure are applied to the problem for the symmetry planes at $z=0$ and 1. In these symmetry planes, the continuity equation is given by (4.13b) which is written as

$$\left\{ \frac{\cos(\pi \hat{\xi}/2) \cos(\pi \hat{\eta}/2)}{\cos(\pi \hat{x}/2) \cos(\pi \hat{y}/2)} \right\}^2 \left[\frac{\partial \hat{x}}{\partial \hat{\xi}} \frac{\partial \hat{y}}{\partial \hat{\eta}} - \frac{\partial \hat{x}}{\partial \hat{\eta}} \frac{\partial \hat{y}}{\partial \hat{\xi}} \right] = J_2 \left(= \frac{1}{\tilde{z}} \right) \quad (\text{A } 6)$$

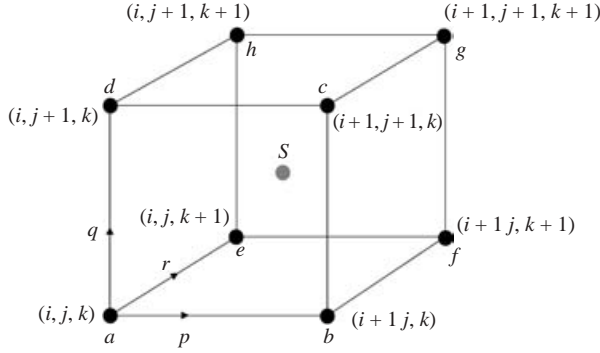


FIGURE 17. Three-dimensional mesh showing a stationary point S ; (p, q, r) are the normalized coordinates used to locate S , measured from (i, j, k) . The mesh size is denoted by $\Delta\hat{\xi}$, $\Delta\hat{\eta}$ and $\Delta\hat{\zeta}$ in the directions p , q and r , respectively.

in terms of the computational variables $\hat{\xi}$ and $\hat{\eta}$; the subsidiary equations along the characteristic curves $\hat{x} = \text{constant}$ are

$$\frac{d\hat{\xi}}{\hat{A}} = \frac{d\hat{\eta}}{\hat{B}} = \frac{d\hat{y}}{\hat{C}} = d\hat{s}, \quad (\text{A } 7a)$$

$$\hat{A} = -\frac{\partial\hat{x}}{\partial\hat{\eta}}, \quad \hat{B} = \frac{\partial\hat{x}}{\partial\hat{\xi}}, \quad \hat{C} = J_2 \left\{ \frac{\cos(\pi\hat{x}/2) \cos(\pi\hat{y}/2)}{\cos(\pi\hat{\xi}/2) \cos(\pi\hat{\eta}/2)} \right\}^2. \quad (\text{A } 7b)$$

For the normal velocity v , the two intermediate functions $\psi(x, y, t)$ and $\phi(x, y, t)$ are now defined as

$$u = \frac{\partial\psi}{\partial y}, \quad v = -\frac{\partial\psi}{\partial x} - \phi, \quad \theta = \frac{\partial\phi}{\partial y}, \quad (\text{A } 8a-c)$$

which satisfy the continuity equation (3.9c) for the symmetry planes, where the appropriate boundary conditions are

$$u = -1 \quad \text{for } \Gamma > 0, \quad u = -\beta \quad \text{for } \Gamma < 0, \quad (\phi, \psi, v, \theta) = 0 \quad \text{at } y = \eta = 0. \quad (\text{A } 9)$$

Once the two intermediate functions ψ and ϕ are calculated in a fashion similar to the three-dimensional case along the characteristic curves associated with computing y , the normal velocity v is defined by (A 8b) throughout the symmetry planes at $z = 0$ and 1.

At each time step, it is necessary to check for the occurrence of a singularity in the interior and on the symmetry planes. A singularity occurs in the interior if

$$\hat{A} = \hat{B} = \hat{C} = 0 \quad \text{at } (\hat{\xi}, \hat{\eta}, \zeta, t) = (\hat{\xi}_s, \hat{\eta}_s, \zeta_s, t_s), \quad (\text{A } 10)$$

where \hat{A} , \hat{B} , \hat{C} and \hat{D} are defined in (A 2). Similarly, a singularity occurs on either symmetry plane if $\hat{A} = \hat{B} = 0$ in (A 7). At any instant t , the entire computational domain must be examined to see if there is a location where \hat{A} , \hat{B} and \hat{C} vanish simultaneously. A typical three-dimensional mesh cell is shown in figure 17. When a stationary point S develops somewhere inside the cell at time $t = t_s$, all three surfaces $\hat{A} = 0$, $\hat{B} = 0$ and $\hat{C} = 0$ touch one another at the location called S . The exact location of S in a three-dimensional mesh will be determined in terms of the normalized local coordinates (p, q, r) shown in the figure 17, where $0 \leq (p, q, r) \leq 1$; the stationary

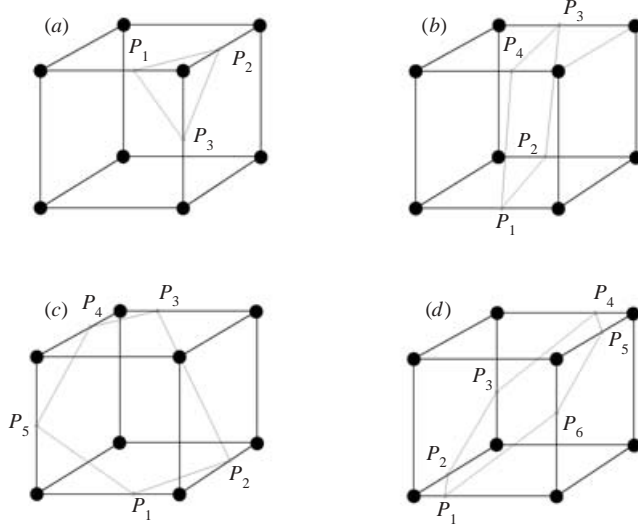


FIGURE 18. Illustrations of the four possible situations for a surface $f=0$ passing through a cell, i.e. a plane intersecting the edges at three, four, five and six points.

point developed at S has the following coordinates

$$\hat{\xi}_s = \hat{\xi}_i + p_s \Delta \hat{\xi}, \quad \hat{\eta}_s = \hat{\eta}_j + q_s \Delta \hat{\eta}, \quad \zeta_s = \zeta_k + r_s \Delta \zeta. \quad (\text{A } 11)$$

Let $f(\hat{\xi}, \hat{\eta}, \zeta)$ denote any of the surfaces \hat{A} , \hat{B} and \hat{C} . Consider then the various possible situations for which the surface $f=0$ can pass through a cell in the three-dimensional mesh. It is assumed that the mesh is sufficiently small so that the surface $f=0$ may be approximated by a plane within the cell. Thus, situations where the surface bends over on itself within an individual cell are excluded from consideration. To determine if the surface $f=0$ passes through a given cell, it is useful to examine whether a change in the sign of f occurs along each edge of the cell, as previously done by Degani *et al.* (1998) for two-dimensional cells. The maximum number of intersections that can be made by $f=0$ along edges of a cell is six and the minimum number of intersections is three (see figure 18).

Suppose that a portion of the surface $f=0$ passes into a cell in the three-dimensional mesh, making three intersections with the edges, as depicted figure 18(a). Let these three points be denoted by $P_1=(p_1, q_1, r_1)$, $P_2=(p_2, q_2, r_2)$ and $P_3=(p_3, q_3, r_3)$, respectively. The equation of a plane passing through three points (P_1, P_2, P_3) in normalized coordinates (p, q, r) is

$$n_1(p - p_1) + n_2(q - q_1) + n_3(r - r_1) = 0, \quad (\text{A } 12)$$

where (n_1, n_2, n_3) are the normals to the plane and defined by

$$n_1 = \begin{vmatrix} q_2 - q_1 & r_2 - r_1 \\ q_3 - q_1 & r_3 - r_1 \end{vmatrix}, \quad n_2 = \begin{vmatrix} r_2 - r_1 & p_2 - p_1 \\ r_3 - r_1 & p_3 - p_1 \end{vmatrix}, \quad n_3 = \begin{vmatrix} p_2 - p_1 & q_2 - q_1 \\ p_3 - p_1 & q_3 - q_1 \end{vmatrix}. \quad (\text{A } 13)$$

Equation (A 12) can be rewritten in the form

$$(p - p_1) + \tilde{n}_2(q - q_1) + \tilde{n}_3(r - r_1) = 0, \quad (\text{A } 14)$$

where $\tilde{n}_2 = n_2/n_1$ and $\tilde{n}_3 = n_3/n_1$. An intersection is detected along an edge of a cell if the product of f with itself evaluated at each corner is negative. The coordinates of

the intersection are then easily obtained. For example, the coordinates of P_1 , P_2 and P_3 shown in figure 18(a) are

$$P_1 : \quad p_1 = \frac{f_{i,j+1,k}}{f_{i,j+1,k} - f_{i+1,j+1,k}}, \quad q_1 = 1.0, \quad r_1 = 0, \quad (\text{A } 15a)$$

for $f_{i,j+1,k}f_{i+1,j+1,k} < 0$,

$$P_2 : \quad p_2 = 1.0, \quad q_2 = 1.0, \quad r_2 = \frac{f_{i+1,j+1,k}}{f_{i+1,j+1,k} - f_{i+1,j+1,k+1}}, \quad (\text{A } 15b)$$

for $f_{i+1,j+1,k}f_{i+1,j+1,k+1} < 0$, and

$$P_3 : \quad p_3 = 1.0, \quad q_3 = \frac{f_{i+1,j,k}}{f_{i+1,j,k} - f_{i+1,j+1,k}}, \quad r_3 = 0, \quad (\text{A } 15c)$$

for $f_{i+1,j,k}f_{i+1,j+1,k} < 0$. If four or more intersections are detected (i.e. $P_1 = (p_1, q_1, r_1)$, $P_2 = (p_2, q_2, r_2)$, $P_3 = (p_3, q_3, r_3)$, $P_4 = (p_4, q_4, r_4), \dots$) in a cell, an approximate plane is defined using average values of the normals. For four intersections (i.e. P_1, P_2, P_3, P_4), for example, a first set of normals, i.e. (n_{1a}, n_{2a}, n_{3a}) , is obtained from the three points (P_1, P_2, P_3) and a second set of normals, i.e. (n_{1b}, n_{2b}, n_{3b}) , is similarly obtained from the three points (P_1, P_2, P_4) . Here, (n_{1a}, n_{2a}, n_{3a}) are given by (A 13) while (n_{1b}, n_{2b}, n_{3b}) are obtained from the same equation, but with (p_3, q_3, r_3) replaced by (p_4, q_4, r_4) . Average normals to the plane are then defined by

$$\tilde{n}_2 = \frac{1}{2}(\tilde{n}_{2a} + \tilde{n}_{2b}), \quad \tilde{n}_3 = \frac{1}{2}(\tilde{n}_{3a} + \tilde{n}_{3b}) \quad (\text{A } 16a)$$

where

$$\tilde{n}_{2a} = \frac{n_{2a}}{n_{1a}}, \quad \tilde{n}_{3a} = \frac{n_{3a}}{n_{1a}}; \quad \tilde{n}_{2b} = \frac{n_{2b}}{n_{1b}}, \quad \tilde{n}_{3b} = \frac{n_{3b}}{n_{1b}}, \quad (\text{A } 16b)$$

for which (A 14) still holds. Similarly, an approximate plane is defined for a cell having five or six intersections.

A singular point is located when (A 14) holds for all three surfaces $\hat{A} = 0$, $\hat{B} = 0$ and $\hat{C} = 0$ simultaneously at a point in the cell, i.e. when

$$(p - p_{1,\hat{A}}) + \tilde{n}_{2,\hat{A}}(q - q_{1,\hat{A}}) + \tilde{n}_{3,\hat{A}}(r - r_{1,\hat{A}}) = 0, \quad (\text{A } 17a)$$

$$(p - p_{1,\hat{B}}) + \tilde{n}_{2,\hat{B}}(q - q_{1,\hat{B}}) + \tilde{n}_{3,\hat{B}}(r - r_{1,\hat{B}}) = 0, \quad (\text{A } 17b)$$

$$(p - p_{1,\hat{C}}) + \tilde{n}_{2,\hat{C}}(q - q_{1,\hat{C}}) + \tilde{n}_{3,\hat{C}}(r - r_{1,\hat{C}}) = 0, \quad (\text{A } 17c)$$

are satisfied and $0 \leq (p, q, r) \leq 1$ at that point. To check for the presence of a singularity and compute the normalized coordinates, (A 17) must be solved for (p, q, r) at any instant. If the calculated values of (p, q, r) are all less than 1, then a singularity has been detected in that cell.

REFERENCES

- ADAMS, E. C., CONLISK, A. T. & SMITH, F. T. 1995 Adaptive grid scheme for vortex-induced boundary layers. *AIAA J.* **33**, 864–870.
- ATIK, H. 2002 Boundary-layer separation and control. PhD thesis, Lehigh University.
- COWLEY, S. J., VAN DOMMELEN, L. & LAM, S. T. 1990 On the use of Lagrangian variables in descriptions of unsteady boundary-layer separation. *Phil. Trans. R. Soc. Lond. A* **333**, 343–378.
- DALLMANN 1988 Three-dimensional vortex structures and vorticity topology. *Japan. Soc. Fluid Dyn., Fluid Dyn. Res.* **3**, 183–189.

- DEGANI, A. T., WALKER, J. D. A. & SMITH, F. T. 1998 Unsteady separation past moving surfaces. *J. Fluid Mech.* **375**, 1–38.
- DHANAK, M. R. & DEBERNARDINIS, B. 1981 The evolution of an elliptic vortex ring. *J. Fluid Mech.* **109**, 189–216.
- DOLIGALSKI, T. L. & WALKER, J. D. A. 1984 The boundary layer induced by a convected vortex. *J. Fluid Mech.* **139**, 1–28.
- ELLIOTT, J. W., COWLEY, S. J. & SMITH, F. T. 1983 Breakdown of boundary layers: (i) on moving surfaces; (ii) in semi-similar flow; (iii) in fully unsteady flow. *Geophys. Astrophys. Fluid Dyn.* **25**, 77–138.
- ERSOY, S. & WALKER, J. D. A. 1987 The boundary layer due to a three-dimensional vortex loop. *J. Fluid Mech.* **185**, 569–598.
- HEAD, M. R. & BANDYOPHADYAY, P. 1981 New aspects of turbulent boundary-layer structure. *J. Fluid Mech.* **107**, 297–337.
- HON, L.-T. & WALKER, J. D. A. 1991 Evolution of a hairpin vortex in a shear flow. *Computers Fluids* **20**, 343–358.
- HOYLE, J. M. & SMITH, F. T. 1994 On finite-time break-up in three dimensional unsteady interacting boundary layers. *Proc. R. Soc. Lond. A* **447**, 467–492.
- KIM, C.-Y. 1999 Unsteady separation phenomena in two- and three-dimensional boundary-layer flows. PhD thesis, Lehigh University.
- LEONARD, A. 1980 Vortex methods in flow simulation. *J. Comput. Phys.* **37**, 289–335.
- LI, L., WALKER, J. D. A., BOWLES, R. I. & SMITH, F. T. 1998 Sort-scale break-up in unsteady interactive layers: local development of normal pressure gradients and vortex wind-up. *J. Fluid Mech.* **374**, 335–378.
- MOORE, D. W. 1972 Finite amplitude waves on aircraft trailing vortices. *Aero. Q.* **23**, 307–314.
- PERIDIER, V. J., SMITH, F. T. & WALKER, J. D. A. 1991 Vortex-induced boundary-layer separation. Part 1. The unsteady limit problem. *J. Fluid Mech.* **232**, 91–131.
- PUHAK, R. I., DEGANI, A. T. & WALKER, J. D. A. 1995 Unsteady separation and heat transfer upstream of obstacles. *J. Fluid Mech.* **305**, 1–27.
- ROBINSON, S. K. 1991 Coherent motions in the turbulent boundary layer. *Annu. Rev. Fluid Mech.* **23**, 601–639.
- SMITH, C. R. & WALKER, J. D. A. 1997 Sustaining mechanisms of turbulent boundary layers: the role of vortex development and interaction. In *Sustaining Mechanisms of Wall Turbulence* (ed. R. L. Panton), pp. 13–39. Computational Mechanics Publications, Southampton.
- SMITH, C. R., WALKER, J. D. A., HAIDAIRI, A. H. & SOBRUN, U. 1991 On the dynamics of near-wall turbulence. *Phil. Trans. R. Soc. Lond. A* **336**, 131–175.
- SMITH, F. T., BOWLES, R. I. & WALKER, J. D. A. 2000 Wind-up of a spanwise vortex in deepening transition and stall. *Theoret. Comput. Fluid Dyn.* **14**, 135–165.
- SMITH, F. T. & BURGGRAF, O. R. 1985 On the development of large-sized short-scaled disturbances in boundary layers. *Proc. R. Soc. Lond. A* **339**, 25–55.
- TOBAK, M. & PEAKE, D. J. 1982 Topology of three-dimensional separated flows. *Annu. Rev. Fluid Mech.* **14**, 61–85.
- VAN DOMMELEN, L. L. 1991 Lagrangian description of unsteady separation. *Lect. Appl. Maths* **28**, 701–718.
- VAN DOMMELEN, L. L. & COWLEY, S. J. 1990 On the Lagrangian description of unsteady boundary-layer separation. Part 1. General theory. *J. Fluid Mech.* **220**, 593–626.
- VAN DOMMELEN, L. L. & SHEN, S. F. 1980 The spontaneous generation of a singularity in a separating boundary layer. *J. Comput. Phys.* **38**, 125–140.
- VAN DOMMELEN, L. L. & SHEN, S. F. 1982 The genesis of separation. In *Symposium on Numerical and Physical Aspects of Aerodynamic Flows* (ed. T. Cebeci), pp. 293–311. Springer.
- WALKER, J. D. A. 1978 The boundary layer due to a rectilinear vortex. *Proc. R. Soc. Lond. A* **359**, 167–188.
- WALKER, J. D. A. 2003 Unsteady separation processes at high Reynolds numbers and their control. *J. Flow Turbulence Combust.* (to appear).
- XIAO, Z., BURGGRAF, O. R. & CONLISK, A. T. 1997 The interacting boundary-layer flow due to a vortex approaching a cylinder. *J. Fluid Mech.* **346**, 319–343.